Materials Today Bio 29 (2024) 101369

Contents lists available at ScienceDirect

Materials Today Bio

journal homepage: www.journals.elsevier.com/materials-today-bio

Microenvironment-responsive injectable hydrogel for neuro-vascularized bone regeneration☆

Wanshun Wang [a,b,f,1], Hu Chen [c,d,1], Jiacong Xiao [e,f,1], Dan Luo [b,f], Yonghui Hou [b,f], Jiheng Zhan [b], Yu Hou [b], Xing Li [b], Huili Yang [h,***], Shudong Chen [b,g,**], Dingkun Lin [b,g,*]

[a] The Second Clinical Medical College, Guangzhou University of Chinese Medicine, Guangzhou 510405, Guangdong, China
[b] Department of Orthopedic Surgery, Guangdong Provincial Hospital of Chinese Medicine, The Second Affiliated Hospital of Guangzhou University of Chinese Medicine, Guangzhou 510120, Guangdong, China
[c] The First School of Clinical Medicine, Southern Medical University, Guangzhou 510515, China
[d] Department of Orthopedics, General Hospital of Southern Theatre Command of PLA, Guangzhou 510010, China
[e] The First Clinical Medical College, Guangzhou University of Chinese Medicine, Guangzhou 510405, Guangdong, China
[f] Lingnan Medical Research Center of Guangzhou University of Chinese Medicine, Guangzhou 510405, Guangdong, China
[g] Chinese Medicine Guangdong Laboratory, Hengqin 519031, Guangdong, China
[h] Department of Hepatology, Shenzhen Traditional Chinese Medicine Hospital, The Fourth Clinical Medical College of Guangzhou University of Chinese Medicine, Shenzhen 518033, Guangdong, China

ARTICLE INFO

Keywords:
Injectable responsive hydrogel
Angiogenesis
Osteogenesis
Neurogenesis
Bone regeneration

ABSTRACT

Bone is a richly innervated and vascularized tissue, whereas nerve-vascular network reconstruction was often ignored in biomaterial design, resulting in delayed or incomplete bone healing. Inspired by the bone injury microenvironments, here we report a controllable drug delivery strategy using a pH and reactive oxygen species (ROS) dual-response injectable hydrogel. Based on the dynamic borate ester bond covalent crosslinking, nano-hydroxyapatite (HA) and curculigoside (CCG) are integrated into PVA/TSPBA (PT) to construct a responsive injectable hydrogel (PTHC), which scavenges excessive ROS from the injury microenvironment and responsively releases HA and CCG, providing favorable homeostasis and *in situ* sustained release drug delivery system for bone repair. Additionally, PTHC hydrogel can alleviate ROS-mediated intracellular oxidative and exhibit multiple biological activities of angiogenesis, neurogenesis, and osteogenesis. Furthermore, it reconstructs the micro-vascular network, accelerates sensory nerve repair, secretes neurotransmitters and bioactive factors, and improves neuro-vascularized bone regeneration. This multi-bioactive injectable hydrogel system offers a promising advance in therapeutic materials for bone repair.

1. Introduction

Severe trauma, degenerative diseases, surgery, and various reasons can lead to the occurrence of bone defects in clinical practice, over two million bone-grafting operations are annually performed worldwide [1, 2]. Although autograft is widely regarded as the gold standard for

☆ This research was financially supported by the National Natural Science Foundation of China (82074451; 81704095; 82104895), the Guangzhou Science and Technology Planning Project (202102020542), the China Postdoctoral Science Foundation (2021M700905), and the Science and Technology Program of Guangzhou (202201010974).

* Corresponding author. Department of Orthopedic Surgery, Guangdong Provincial Hospital of Chinese Medicine, The Second Affiliated Hospital of Guangzhou University of Chinese Medicine, No. 111 Dade Road, Guangzhou 510120, Guangdong, China.
** Corresponding author. Department of Orthopedic Surgery, Guangdong Provincial Hospital of Chinese Medicine, The Second Affiliated Hospital of Guangzhou University of Chinese Medicine, No. 111 Dade Road, Guangzhou 510120, Guangdong, China.
*** Corresponding author. Department of Hepatology, Shenzhen Traditional Chinese Medicine Hospital, The Fourth Clinical Medical College of Guangzhou University of Chinese Medicine, No. 1 Fuhua Road, Shenzhen 518033, Guangdong, China.
E-mail addresses: yhl_phd@163.com (H. Yang), chenshudong_med@163.com (S. Chen), lindingkuntcm@126.com (D. Lin).
[1] Wanshan Wang, Hu Chen, and Jiacong Xiao are co-first authors.

https://doi.org/10.1016/j.mtbio.2024.101369
Received 5 September 2024; Received in revised form 7 November 2024; Accepted 24 November 2024
Available online 26 November 2024
2590-0064/© 2024 The Authors. Published by Elsevier Ltd. This is an open access article under the CC BY-NC-ND license (http://creativecommons.org/licenses/by-nc-nd/4.0/).

treating bone defects, it presents a series of problems including limited source, donor site injury, shape mismatch, and potential risk of infection, making bone repair a major challenge in surgical management [3,4]. Severe bone injury can result in changes to the microenvironment, such as increased reactive oxygen species (ROS), decreased pH, inadequate blood supply, and mechanical instability [5]. As one of the important factors regulating the pathophysiological microenvironment of bone tissue, ROS accumulates in bone defect sites and impairs cell activity through oxidative stress response, thereby inhibiting bone healing [6,7]. Hence, scavenging excessive ROS in the bone injury microenvironment facilitates the repair of bone defects.

Currently, despite huge advances in bone tissue engineering biomaterials as an alternative to autografts, the insufficient vascularization and innervation of bone regeneration continue to pose a main obstacle [8,9]. Bone development and repair are closely related to the growth and function of vascular networks and sensory nerve fibers [10,11]. Abundant blood vessels accompanied by nerve fibers are distributed in the Haversian and Volkmann canals of bone tissue, maintaining adequate blood supply and providing essential nutrients and growth factors for bone formation [12]. Also, bones are innervated by peripheral sensory nerves in the nerve-bone axis, and neurotrophic factors are involved in regulating osteogenesis [13]. Therefore, neurovascular regeneration plays a key role in promoting bone healing. Interestingly, nano-hydroxyapatite (HA), the most widely used bone repair material with a similar calcium-phosphorus ratio to bone, has been reported to promote nerve differentiation and neuronal maturation [14,15]. More importantly, Curculigoside (CCG), a major natural compound extracted from the rhizomes of Curculigo orchioides Gaertn, exhibits a wide spectrum of biological activities such as anti-oxidation, anti--osteoporosis, nerve protection, pro-osteogenesis, and pro-angiogenesis [16–19]. However, the clinical application of this effective natural compound in the treatment of bone defects is limited by its low solubility, poor stability, short drug half-life, and excessive metabolic rate. Bone tissue engineering hydrogels can not only avoid the problems of insufficient solubility and low bioavailability in the application of herbal monomers but also take into account the need for high biocompatibility.

To this end, we take advantage of the responsiveness and functionality of injectable PVA/TSPBA (PT) hydrogel, strong mechanical properties of osteoinductive HA, and multiple biological activities of natural CCG, to prepare pH and ROS dual-response injectable hydrogel referred to as PVA/TSPBA/HA/CCG (PTHC) for regulating the injury microenvironment in the bone defects region. The dynamic covalent borate ester bond between the boric acid and hydroxyl groups not only provides ROS scavenging ability and injectable portability for PT-based hydrogels but also enables microenvironment-responsive release of HA and CCG. By combining natural pharmaceutical molecules and responsive biomaterials, the system overcomes the disadvantage of the short half-life of CCG and achieves prolonged efficacy and on-demand release *in vivo*. Furthermore, the pH- and ROS-responsive release of HA and CCG from PTHC hydrogel could enhance angiogenesis, neurogenesis, and osteogenesis, as well as accelerate neuro-vascularized bone regeneration (Scheme 1). This dynamically controllable drug delivery strategy efficiently improved the damaged microenvironment and promoted bone healing of the critical-sized bone defect model with only a single hydrogel injection.

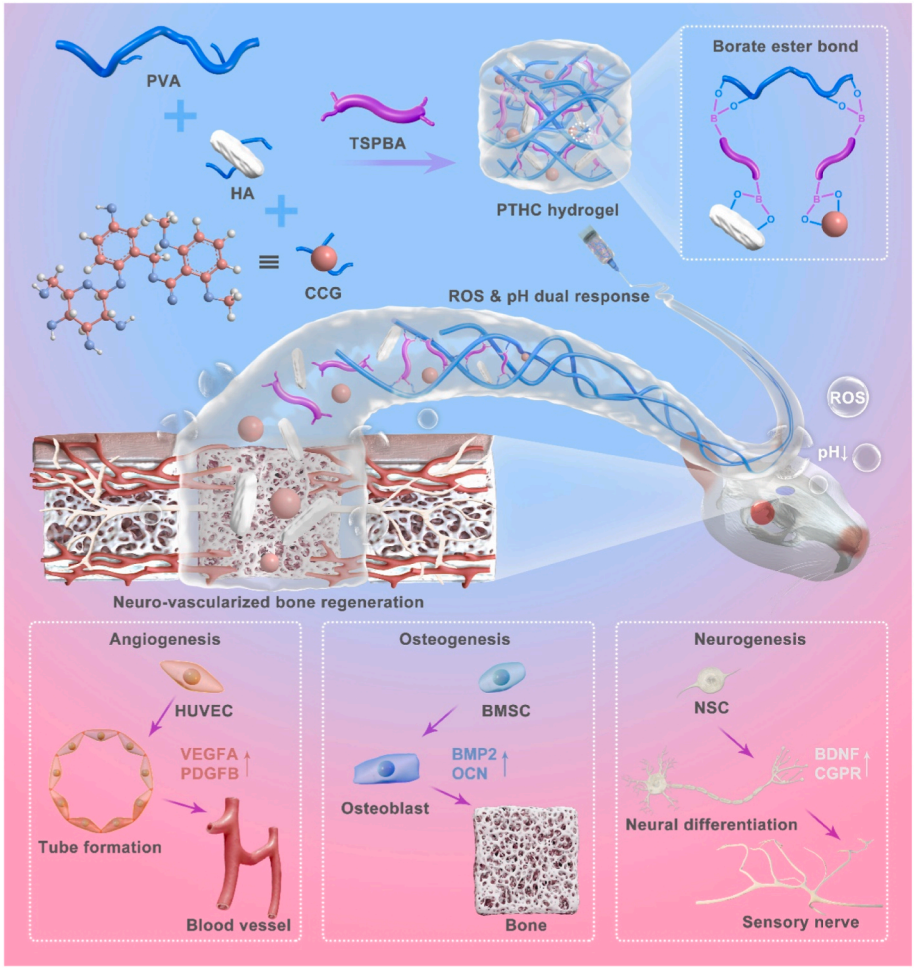

Scheme 1. Schematic illustration of the fabrication of pH and ROS dual-response multi-bioactive PTHC hydrogel for neuro-vascularized bone regeneration.

2. Materials and methods

2.1. Materials and cells

N, N, N′, N′-Tetramethyl-1,3-propanediamine (TMPDA), 4-(Bromomethyl)phenylboronic acid (BPBA), N, N-dimethylformamide (DMF), tetrahydrofuran (THF), CCG, nano-HA, polyvinyl alcohol (PVA), deuterium oxide (D_2O), potassium bromide (KBr), 2-Phenyl-4,4,5,5-tetramethylimidazoline-3-oxide-1-oxyl (PTIO), and hydrogen peroxide (H_2O_2) were purchased from Shanghai Macklin Biochemical Technology Co., Ltd. (China). Human venous endothelial cells (HUVECs), rat bone mesenchymal stem cells (BMSCs), and rat neural stem cells (NSCs) were purchased from Cyagen Biosciences Guangzhou Inc. (China).

2.2. Preparation of hydrogels

Briefly, 0.2 g TMPDA and 1 g BPBA were added into 50 mL DMF solution and stirred at 60 °C for 12 h. Next, 100 mL THF was added to the mixture to produce a white solid precipitate, which was collected and lyophilized to obtain N1-(4-boronobenzyl)-N3-(4-boronophenyl)-N1, N1, N3, N3-tetramethylpropane-1, 3-diaminium (TSPBA). Subsequently, 2 g nano-HA, with or without 1 g CCG, was added into 100 mL 16 wt% PVA solution and stirred for 24 h. PVA, PVA/HA, and PVA/HA/CCG were mixed with 6 wt% TSPBA solution in an equal volume to gain PT, PTH, and PTHC hydrogels. The detailed compositions of various PT-based hydrogels were shown in Table S1.

2.3. Characterization

^{1}H nuclear magnetic resonance (^{1}H NMR) spectra of TSPBA in D_2O were recorded using a NMR spectrometer (Avance NEO 400 MHz, Bruker, Germany). The internal morphology and structure of the freeze-dried PT, PTH, and PTHC hydrogels were observed by scanning electron microscopy (SEM, Gemini 300, Zeiss, Germany). Image J software further measured and calculated the pore area, size, and porosity rate. The elemental compositions of the PTHC hydrogel were detected by an energy-dispersive X-ray spectroscopy (EDS, XFlash®, Bruker, Germany). Fourier transform infrared (FTIR) spectra of the hydrogels were measured in the 4000-400 cm^{-1} range with the KBr-disk method using a FTIR spectrometer (Nicolet iN10, Thermo Scientific, USA). Zeta potential of the HA, PT, PTH, and PTHC was measured using a laser nanometer particle size analyzer (Zetasizer Nano ZS90, Malvern, UK).

2.4. Self-healing and mechanical property

The self-healing phenomenon was macroscopically observed at ambient temperature. A disc-shaped PTHC hydrogel was cut into half and then two pieces were contacted to each other for 10 min without any external stimulus. The healing process was validated by stretching the hydrogel to determine its ability to withstand without splitting.

Mechanical properties of the PT, PTH, and PTHC hydrogels were evaluated by rheological, tensile, compressive, and fatigue resistance tests. For the rheological test, the disc-shaped hydrogels were performed on a rheometer (ARES-G2, TA Instruments, USA). The gelation time was detected under a constant strain of 10 % to record the change of storage and loss modulus (G′ and G″) within 10 min. The frequency sweep rheological analyses were evaluated in the linear viscoelastic region with an angular frequency range of 0.1–100 rad s^{-1} at room temperature. For the tensile test, the tensile modulus of rectangle hydrogels with a length of 60 mm and a width of 20 mm were detected using an electronic universal testing machine (LD22.102, LiShi, China). The tensile strain ranged from 0 % to 60 % at a speed of 10 mm min^{-1}. For the compressive test, the compressive modulus of cylindrical hydrogels with a diameter of 13 mm and a height of 10 mm were measured with a compressive strain ranging from 0 % to 80 %. For the fatigue resistance test, PTHC hydrogel was further conducted between 0 % and 30 % strain ranging for 30 cycles over time.

2.5. ROS scavenging ability

PTIO assay was used to assess the ROS scavenging ability of the hydrogel as previous studies [20,21]. Briefly, 1.5 mg of PTIO powder was dissolved in 10 mL of ddH_2O, and the different hydrogel samples were added for 24 h. The absorbance was recorded using a microplate reader (Multiskan GO, Thermo Scientific, USA). The ROS scavenging ability was further calculated at different time points using the following formula:

$$\text{ROS scavenging activity } (\%) = \frac{(A_{PTIO} - A_{sample})}{A_{PTIO}} \times 100 \quad (1)$$

Here, A_{PTIO} is the absorbance of the PTIO solution at 557 nm, and A_{sample} is the absorbance of the reaction products after hydrogel immersion from 0 to 24 h.

2.6. Responsive degradation performance

To evaluate the ROS-responsive degradation behavior of the hydrogels, various hydrogels were respectively soaked in H_2O_2 (100 μM) and phosphate-buffered saline (PBS, pH = 7.4, Gibco, USA) solution for 30 days at 37 °C. The weight of the hydrogel was monitored after drying its surface with absorbent paper, and a fresh solution was replaced every 2 days. The formula for the degradation rate is as follows:

$$\text{Degradation rate } (\%) = \frac{(W_{original} - W_{sample})}{W_{original}} \times 100 \quad (2)$$

Here, $W_{original}$ is the original weight of the hydrogel, and W_{sample} is the weight of the hydrogel after immersion from 1 to 30 days.

2.7. Responsive release performance

The ROS and pH-responsive release behavior of PTHC hydrogel was evaluated by soaking in H_2O_2 (100 μM) and PBS (pH = 7.4 and 6.5) solution for 30 days at 37 °C. The concentration of nano-HA was measured using nanoparticle tracking analysis (NTA, Nanosight NS300, Malvern, UK), and the concentration of CCG was detected via high performance liquid chromatography (HPLC, LC-20A, SHIMADZU, Japan) with a chromatographic column (4.6 mm × 250 mm, 5 μm) at 285 nm. The formula for the release rate is as follows:

$$\text{Release rate } (\%) = \frac{C_{time}}{C_{original}} \times 100 \quad (3)$$

Here, $C_{original}$ is the original concentration of nano-HA or CCG, and C_{time} is the concentration of nano-HA or CCG at different time points.

2.8. Biocompatibility assay in vitro

To evaluate the cytocompatibility of hydrogel, HUVECs were co-cultured with various hydrogels in high glucose DMEM medium (Gibco, USA) containing 10 % FBS and 1 % penicillin-streptomycin for 1, 3, and 5 days. The cytotoxicity and proliferation of the HUVECs were detected using cell counting kit 8 (CCK-8, Dojindo, Japan), and the optical density (OD) values were measured at 450 nm by a microplate reader. Meanwhile, the HUVECs were stained by a live/dead staining kit (BB-4126, Bestbio, China) and observed using a fluorescence microscope (Leica, Germany). The hemocompatibility assay was conducted following the previous study [22]. In brief, ddH_2O, PBS, and hydrogels were mixed with PBS-diluted blood and incubated at 37 °C for 1 h. After centrifuging the mixture and collecting the supernatant, the OD values were measured at 545 nm using a microplate reader. The formula for the hemolysis ratio is as follows:

$$\text{Hemolysis rate}\ (\%) = \frac{(OD_{sample} - OD_{PBS})}{(OD_{ddH_2O} - OD_{PBS})} \times 100 \quad (4)$$

Here, OD_{ddH2O} and OD_{PBS} are the OD values of blood supernatant treated by ddH_2O and PBS solution, and OD_{sample} is the OD value of blood supernatant treated by different hydrogels.

2.9. Angiogenesis assay in vitro

To investigate the effect of hydrogels on cell migration, a cell wound scratch assay was performed following the previous study [23]. After the cell layer was scratched, HUVECs were co-cultured with hydrogels for 24 h, and then stained with a live/dead cell staining kit. As for the tube formation assay, HUVECs were seeded and adhered to the matrigel (082704, ABW, China), and then co-cultured with different hydrogels for 6 h. The cytoskeleton was stained with a Phalloidin staining kit (BB-441426, Bestbio, China), and the nucleus was stained by DAPI (C1005, Beyotime, China). After photographing the images with a fluorescence microscope, the cell migration distance, tube length, and number of vessels and meshes were measured using the Image J software.

The gene expression levels of platelet endothelial cell adhesion molecule-1 (CD31) and vascular endothelial growth factor A (VEGFA) were evaluated by quantitative real time-polymerase chain reaction (qRT-PCR). RNA was extracted using NucleoZOL (MNG, Germany) and quantified with an ultra-microvolume spectrophotometer (OSE260, Tiangen, China), and then reverse-transcribed to cDNA using a reverse transcription cDNA synthesis kit (04897030001, Roche, Germany). The synthesized cDNA and primers were mixed with SYBR Green Master Mix (DBI-2043, DBI Bioscience, Germany) to detect the gene expression. The $2^{-\Delta\Delta Ct}$ method was used for quantitative calculation. All the primer sequences in this study have been listed in Table S2.

In addition, immunofluorescence (IF) staining was used to detect the expression of angiogenesis-related proteins on HUVECs after 3 days of different treatments. Briefly, after fixation and penetration, cells were blocked with 5 % BSA and incubated with the primary antibodies of CD31(ER31219, HUABIO) and VEGFA (ET1604-28, HUABIO) at 4 °C overnight. Fluorescently labeled secondary antibody (HA1122, HUABIO, China) was then added and incubated for 1 h. Afterward, the HUVECs were stained by DAPI and observed using a fluorescence microscope. ImageJ software was used to quantify the fluorescence intensity of cells.

2.10. Osteogenesis assay in vitro

To evaluate the effect of hydrogels on osteogenic differentiation, BMSCs were co-cultured with various hydrogels in the osteogenic induction medium (RAXMX-90021, OriCell, China) for 7 and 14 days. After 7 days of treatment, alkaline phosphatase (ALP) activities of BMSCs were determined using an ALP assay kit (P0321S, Beyotime, China). Meanwhile, BCIP/NBT solution (C3206, Beyotime, China) was used for ALP staining. After 14 days of osteogenesis induction, BMSCs were stained with an alizarin red S (ARS, ALIR-1001, OriCell, China) staining solution. Macro and micro images were photographed with a digital camera and a microscope. For quantitative analysis of ARS staining, the calcium deposits were dissolved by 10 % cetylpyridinium chloride (Sigma, USA) and detected at 562 nm using a microplate reader. In addition, the expression levels of osteoblast-related genes including bone morphogenetic protein 2 (BMP2), RUNX family transcription factor 2 (RUNX2), osteopontin (OPN), and osteocalcin (OCN) were evaluated by qRT-PCR. The expression levels of BMP2 (ER80602, HUABIO) and OCN (ER1919-20, HUABIO) on BMSCs were further assessed by IF staining.

2.11. Neural differentiation assay in vitro

To assess the effect of hydrogels on neural differentiation, NSCs were co-cultured with various hydrogels in the neurobasal medium (Gibco, USA) containing 2 % B-27 for 7 days. After neural differentiation induction, the expression levels of neuron-related genes including tubulin beta-III (TUBB3) and microtubule-associated protein 2 (MAP2) were detected by qRT-PCR. Meanwhile, the expression levels of TUBB3 (ET1604-17, HUABIO) and MAP2 (HA500177, HUABIO) on NSCs were evaluated by IF staining. After capturing images with a fluorescence microscope, Sholl analysis, dendrite length, and number of neurites were quantified using ImageJ software.

2.12. ROS detection in vitro

To evaluate the effect of hydrogels on intracellular ROS scavenging, H_2O_2-induced HUVECs, BMSCs, and NSCs were respectively co-cultured with hydrogels for 1 h. The cells were incubated with 2, 7-dichlorodihydrofluorescein diacetate (DCFH-DA, ID3130, Solarbio) at 37 °C for 30 min, and then observed using a fluorescence microscope. ImageJ software was used to quantify the fluorescence intensity of cell products.

2.13. Bone defect model

All the animal experiments were performed on male Sprague Dawley (SD) rats (180–220 g, 6 weeks old) and approved by the Institutional Animal Care and Use Committee of the General Hospital of Southern Theatre Command of PLA with a permit number SYDW2022096. The experimental protocols followed the Guidelines for the Care and Use of Laboratory Animals from the National Institutes of Health. SD rats were randomly divided into four groups with six rats in each group: control, PT, PTH, and PTHC. The protocol of the bone defect model was based on the previous study [24]. In brief, the skin of the anesthetized SD rats was cut along the median line to expose the skull, which was then drilled with two 5 mm diameter holes. After removing the bone, the hydrogels were injected and filled with the defect (Fig. S7). Ultimately, the incision was closed and the skin was sutured. Meanwhile, PT-based hydrogels were injected subcutaneously for *in vivo* degradation analysis. The SD rats were euthanized at 8 weeks after surgery for further experimental analysis.

2.14. Bone and vascular reconstruction

As for the micro-computed tomography (micro-CT) analysis, the skull of SD rats was scanned by micro-CT (Aloka LCT-200, Hitachi, Japan). Meanwhile, 10 U mL^{-1} heparin sodium saline and microfil compounds (MV120 Blue, Flow Tech, USA) were used for angiography at a resolution of 48 μm, rotation angle of 360°, and voltage of 80 kV. Three-dimensional (3D) images of bones and blood vessels were reconstructed by 3D Slicer software. Bone and vascular quantification were further analyzed using CTan software.

2.15. ELISA detection

The fresh blood of SD rats in each group was collected, and then serum was collected after centrifugation at 4 °C. According to the manufacturer's instructions, the secretion of BMP2, OCN, VEGFA, platelet-derived growth factor (PDGF) B, brain-derived neurotrophic factor (BDNF), and calcitonin gene-related peptide (CGRP) was detected by BMP2 (HB765-Ra), OCN (HB759-Ra), VEGFA (HB184-Ra), PDGFB (HB146-Ra), BDNF (HB500-Ra) and CGRP (HB646-Ra) ELISA kits, which were purchased from Shanghai hengyuan biological technology Co., Ltd (China).

2.16. Histological analysis

Calvarial tissues, visceral organs, and skins from various groups of SD rats were collected at 8 weeks postoperatively and then fixed with 4 % paraformaldehyde. The decalcified bone tissues were embedded in paraffin and cut into 5 μm sections, which were routinely dewaxed, hydrated for Hematoxylin and Eosin (H&E), Masson, and Goldner staining, as well as subsequent immunostaining. Meanwhile, the heart, liver, spleen, lung, kidney, and skin from each group were performed H&E staining. The stained sections were scanned by a microscope slides scanner (PANNORAMIC MIDI II, 3DHISTECH, Hungary).

2.17. Immunostaining analysis

The expression of BMP2 and OCN was detected using immunohistochemistry (IHC) staining as previously described [25]. Primary antibody BMP2 (500231, ZENBIO) and OCN (614487, ZENBIO) were used to incubate sections at 4 °C overnight, followed by secondary antibody at 37 °C for 1 h. After color development with the DAB substrate system (AR1022, Boster, China), the nuclears were stained with hematoxylin. As for IF staining, after routine dewaxing, hydration, antigen retrieval, and blocking, the sections were incubated at 4 °C overnight with primary antibody CD31 (M1511-8, HUABIO), VEGFA (R380739, ZENBIO), TUBB3 (R23618, ZENBIO), and MAP2 (250035, ZENBIO) and then incubated with corresponding fluorochrome-conjugated secondary antibody. DAPI was used for nuclear staining. An optical and fluorescence microscopy photographed all the immunostaining of bone tissues, and ImageJ software quantified the IHC and IF staining.

2.18. Transcriptome sequencing

The tissues from the calvarial defect of SD rats in the control and PTHC group (n = 3) were frozen and ground in liquid nitrogen, of which total RNA was extracted using TRIzol (Invitrogen, USA) and then reverse transcribed into cDNA. Illumina HiSeq X10 was used to sequence the cDNA library established after amplification and purification. The relative expression level of mRNA was defined by Fragments per kilobase of exon model per million mapped reads (FPKM). Differential mRNA expression was analyzed by edgeR on R software with the filter criteria of $|\log2FC| \geq 0.5$ and q value < 0.05. Gene ontology (GO) and KEGG enrichment analyses of differentially expressed mRNA were performed on the DAVID website (https://david.ncifcrf.gov/), and the heatmap, volcano plot, and bubble chart were drawn on Bioinformatics (https://www.bioinformatics.com.cn/). Protein-protein interaction (PPI) networks were analyzed using the STRING database and Cytoscape 3.10.2 software to depict the network structures of interactions among differential expression genes (DEGs).

2.19. Western blot analysis

As for the western blot (WB) analysis, equal amounts (30 μg) of each protein suspension from bone tissue were separated on an 8 % SDS-PAGE gel and transferred onto polyvinylidene fluoride membranes. Membranes were subsequently blocked with 5 % skim milk for 1 h before being incubated with primary antibodies phospho-phosphatidylinositol 3-kinase (p-PI3K, 1:1000, HA721672, HUABIO), PI3K (1:1000, ET1608-70, HUABIO), p-Akt (1:1000, ET1607-73, HUABIO), and Akt (1:2000, ET1609-47, HUABIO) at 4 °C overnight. A specific secondary antibody was added to the membranes for 1 h. Immunoreactive bands were visualized by a ChemiDoc MP Imaging System (Bio-Rad). Total protein analysis was performed using ImageJ software.

2.20. Statistical analysis

All experimental results were expressed as mean ± standard deviations (SD). The statistical comparisons among groups were analyzed by one-way analysis of variance followed by Tukey's post hoc test using the SPSS 20.0 software (IBM, USA). The $^{*}p < 0.05$ and $^{**}p < 0.01$ were regarded as statistically significant differences.

3. Results and discussion

3.1. Synthesis and characterization of PTHC hydrogel

The microenvironment-responsive injectable PTHC hydrogel was prepared by PVA, TSPBA, HA, and CCG according to the synthesis routes in Fig. 1A, where the molecular structure of TSPBA was confirmed by ^{1}H NMR (Fig. S1). As shown in Fig. 1B, PTHC hydrogel could be injected as the letters "PTHC" without causing needle blockage and shaped by a five-starred mold, indicating hydrogel possessed injectable and moldable properties, which were beneficial for filling and repairing the irregular bone defect [26]. The self-healing and anti-stretching properties of PTHC hydrogel were demonstrated by the resistance to stretching after two halves of the hydrogel were reconnected (Fig. 1C). Also, the toughness of PTHC hydrogel was verified by knotting and unhitching (Fig. 1D). SEM analysis revealed the presence of porous microstructures inside the PT, PTH, and PTHC hydrogels (Fig. 1E). The addition of HA resulted in a large number of coarse particles with hyperintensity observed in the PTH and PTHC hydrogels, indicating that HA was not just encapsulated in the pores but mainly bounded with hydrogels, which was necessary for the sustained release of HA [27]. Meanwhile, the porosity, pore size, and area distributions of hydrogels were intuitively exhibited in Fig. 1H–J. Furthermore, the elemental distributions and contents of PTHC hydrogel were characterized by EDS (Fig. 1F and G). The results showed that the PTHC hydrogel contained carbon (49.32 ± 1.73 %), oxygen (46.20 ± 1.45 %), phosphorus (1.29 ± 0.12 %), and calcium (2.99 ± 0.26 %), respectively. It is well known that the HA surface featured hydroxyl (−OH) and phosphate groups (PO_4^{3-}) [28]. According to the FTIR analysis in Fig. 1K, the characteristic peak at 1041 cm^{-1} of PO_4^{3-} demonstrated that PTH and PTHC hydrogels contained HA. The peak at 1724 cm^{-1} of C=O proved that CCG was successfully introduced into the PTHC hydrogel. It was also shown that the boric acid group ($-B(OH)_2$) characteristic peak of TSPBA was located at 1377 cm^{-1}, suggesting the successful synthesis of PT-based hydrogels. The evidence indicated that the binding of −OH from PVA, HA, and CCG to TSPBA primarily occurred by borate ester bonds. In addition, based on the zeta potential results in Fig. S2, there was physical electrostatic adsorption between HA and PT-based hydrogels.

Although current bone tissue engineering hydrogels may not be able to replace conventional metal implants as the main load-bearing support materials, hydrogels with sufficient mechanical strength are essential for filling defects and fixing fracture fragments [29,30]. As illustrated in Fig. 2A and S3, rapid cross-linking and sol-gel transition of PTHC hydrogel could be achieved by mixing PVA/HA/CCG with TSPBA. Particularly, the gelation time of PT-based hydrogels was less than 80 s (Fig. 2B). Meanwhile, the oscillatory rheology of various hydrogels was performed by frequency scanning to investigate their stability and viscoelasticity. The results in Fig. 2C and D displayed that $G' > G''$ in PT, PTH, and PTHC hydrogel, manifesting that all PT-based hydrogels possessed good stability. Also, the elastic modulus of PTH and PTHC hydrogels significantly improved with the addition of HA. The tensile and compressive stress-strain curves and modulus of hydrogels were illustrated in Fig. 2E–H. The results showed that the compressive modulus of PTH and PTHC hydrogels (232.80 ± 98.01 and 227.10 ± 95.69 kPa) were significantly higher than that of PT hydrogel (65.18 ± 29.31 kPa), whereas the tensile modulus of different hydrogels without statistically significant differences. It was proved that adding HA nanoparticles could improve the mechanical properties of hydrogel. The compression modulus of the hydrogel was reported to be suitable for non-load-bearing bone repair in the range of 200–500 kPa [31,32]. Compression and release cycle tests further indicated that PTHC

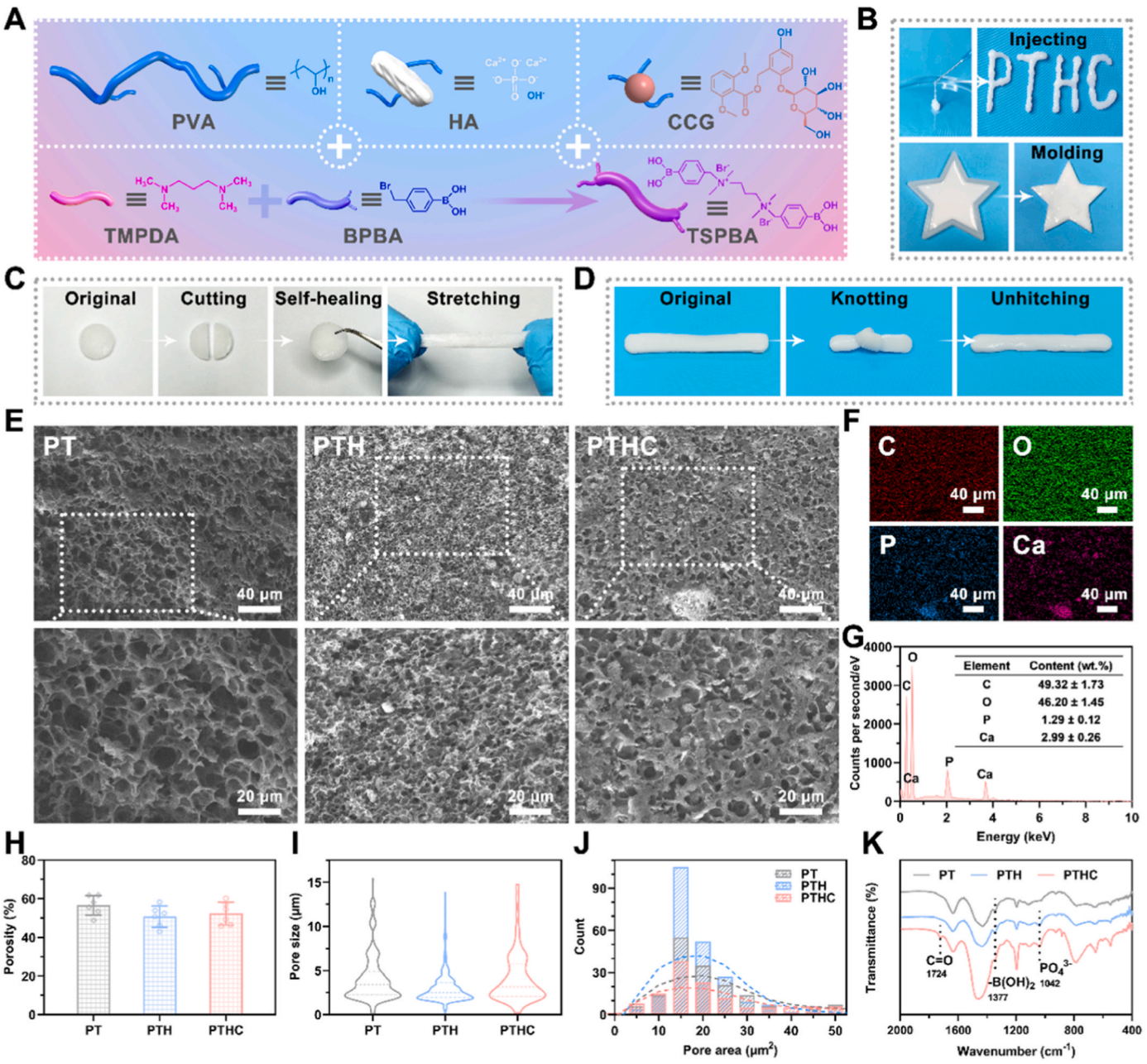

Fig. 1. The synthesis and characterization of PTHC hydrogel. (A) The schematic illustrated the synthesis process of PTHC hydrogel. (B) The injectability and mouldability of PTHC hydrogel. (C, D) PTHC hydrogel exhibited self-healing and anti-stretching properties and revealed toughness via knotting and unhitching. (E) SEM images of PT, PTH, and PTHC hydrogel with different magnifications. (F, G) Mapping images and EDS analysis of PTHC hydrogel. (H–J) Porosity, pore size, and area distributions. (K) FTIR spectra of PT, PTH, and PTHC hydrogel.

hydrogel had excellent fatigue-resistant ability (Fig. 2I and S4), which was beneficial in providing mechanical support during bone repair.

After the bone injury, excessive ROS, such as H_2O_2, is produced due to oxidative stress, which can delay the bone tissue repair process [6,7]. Therefore, scavenging ROS is crucial to improve the bone injury microenvironment. ROS scavenging ability of PT-based hydrogels was performed by PTIO assay in Fig. 2J and K. The results showed that the ROS scavenging effect of PTHC hydrogel was obviously better than that of PT and PTH hydrogels, demonstrating that CCG could synergistically enhance the ROS scavenging activity of PT-based hydrogels. As shown in Fig. 2L, ROS responsive degradation performance of PT-based hydrogels was further confirmed under the H_2O_2 simulated ROS microenvironment within 30 days. Notably, borate ester-bonded PTHC hydrogel exhibited pH and ROS dual-response release behavior in Fig. 2M–P. It is well known that early bone injury presents a slightly acidic physiological microenvironment (pH ≈ 6.5), whereas the microenvironment of healthy bone tissue is weakly alkaline (pH ≈ 7.4) [33]. The results in this study manifested that the release of HA and CCG from PTHC hydrogel was faster in an acidic environment than in a weakly alkaline environment. Also, ROS-sensitive PTHC hydrogel displayed accelerated HA and CCG release in the H_2O_2 solution. Such acid and H_2O_2-accelerated HA and CCG release performance was ascribed to the pH and ROS dual-response borate ester bond, which could lead to the disruption of dynamic covalent interactions between −OH and TSPBA. It was reported that ROS scavenging and responsive hydrogels facilitated the regulation of bone injury microenvironment [7,34].

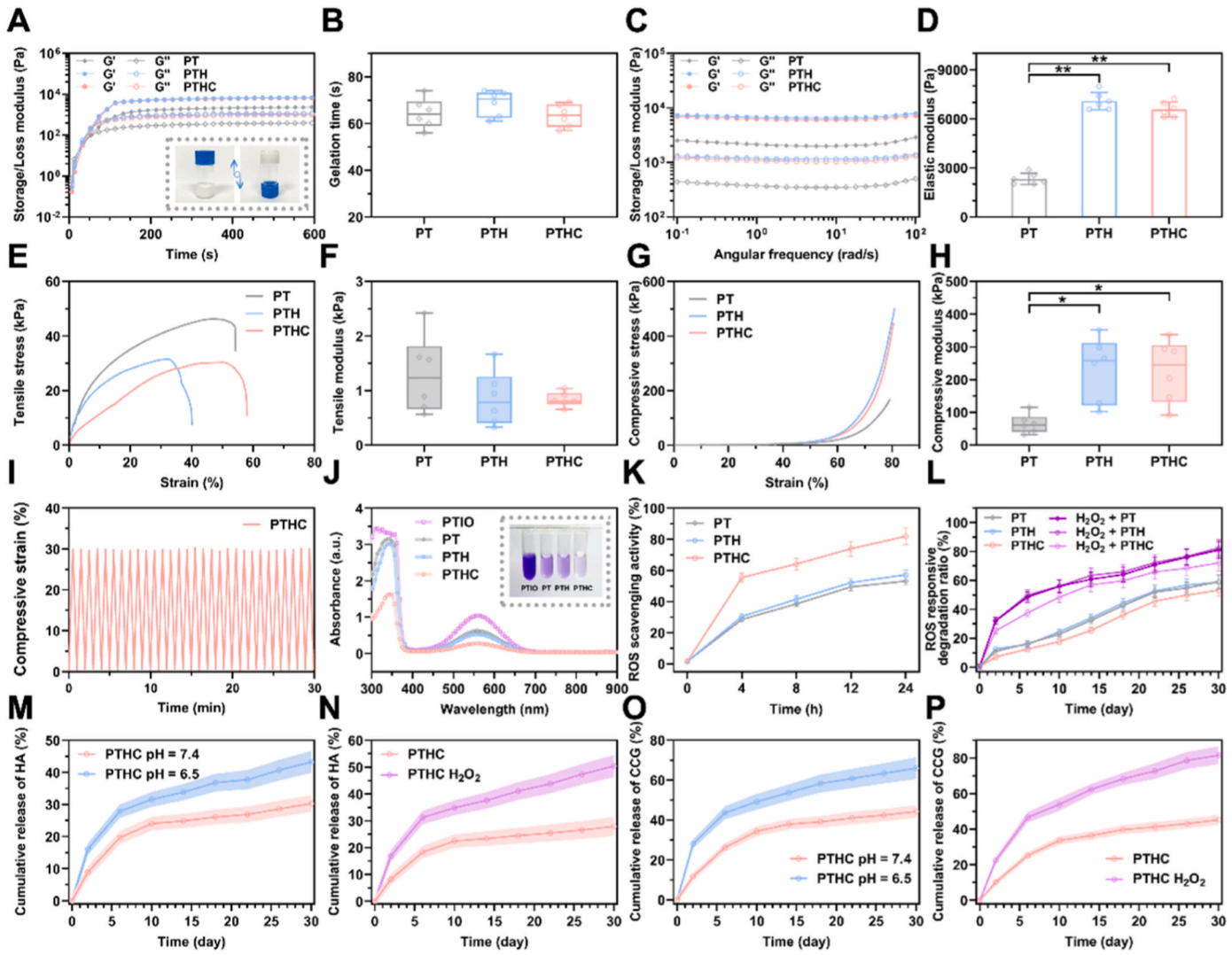

Fig. 2. Mechanical properties and responsive release of PTHC hydrogel. (A, B) Rheological dynamic time scanning and the gelation time. Insert: the photographs of PTHC hydrogel after gelation. (C, D) Rheological dynamic frequency scanning and the elasticity modulus. (E, F) Tensile curves and tensile modulus. (G, H) Compressive curves and compressive modulus. (I) Compressive fatigue resistance of PTHC hydrogel. (J, K) The absorbance curves and ROS scavenging ratio in PTIO assay. Insert: the photograph of PTIO scavenging. (L) ROS responsive degradation ratio of PT, PTH, and PTHC hydrogels treated with and without H_2O_2 solution. (M, N) The release profile of HA from PTHC hydrogel in PBS (pH 7.4 and 6.5) and H_2O_2 solution. (O, P) The release profile of CCG from PTHC hydrogel in PBS (pH 7.4 and 6.5) and H_2O_2 solution. Data were represented as mean ± SD ($n = 6$); $^*p < 0.05$, $^{**}p < 0.01$ compared to the PT group.

3.2. Angiogenic, osteogenic, and neurogenic bioactivities of PTHC hydrogel in vitro

The cytotoxicity and proliferation of PT-based hydrogels were evaluated using live/dead staining and CCK-8 kit on HUVECs and BMSCs (Figs. S5 and S6). The results showed that the PT, PTH, and PTHC hydrogels did not affect the activity and proliferation of HUVECs and BMSCs. The hemocompatibility of the hydrogels was assessed using the hemolysis test in Fig. S7. The hemolysis rate of all hydrogels was less than 5 %, and there was no hemolysis reaction. These results suggested that PT-based hydrogels exhibited good biocompatibility *in vitro*.

Scratched healing and tube formation assay were performed on HUVECs to investigate the effect of hydrogels on angiogenesis *in vitro*. According to the fluorescent images in Fig. 3A, the PTHC hydrogel evidently enhanced the migration and intercellular connections of HUVECs and facilitated the formation of vascular-like structures. HUVECs migration ratio was promoted after treatment with PTHC hydrogel for 24 h (Fig. 3B). Similarly, the tube length and the number of meshes and junctions in the PTHC group were significantly higher than those in the other groups (Fig. 3C–E). Angiogenesis-related VEGFA and CD31 were further detected by qRT-PCR at the gene level (Fig. 3F–G). The results demonstrated that the expression of VEGFA and CD31 on HUVECs treated with PTHC hydrogel was significantly increased compared to other groups. Moreover, IF staining in Fig. 3H–J showed that the VEGFA and CD31 expression in the PTHC group was significantly improved with the release of CCG, which was consistent with qRT-PCR results. The results revealed that the PTHC hydrogel could improve angiogenesis *in vitro*, which was attributed to the angiogenic activity of CCG [19].

ALP level and extracellular matrix mineralization are crucial for evaluating osteogenic activity *in vitro*. As illustrated in Fig. 4A–C, the PTH and PTHC hydrogels could significantly enhance ALP expression and extracellular mineralized crystals on BMSCs compared with the control and PT groups. In particular, the ALP activity of the PTHC group was about twice that of the PTH group. Also, the OD value of calcium crystals in the PTHC group was higher than that in the PTH group. Furthermore, osteogenic differentiation on BMSCs treated with PT-based hydrogels was evaluated using qRT-PCR and IF staining. In comparison to the control and PT groups, osteogenesis-related genes BMP2, RUNX2, OPN, and OCN expressions in the PTH and PTHC groups

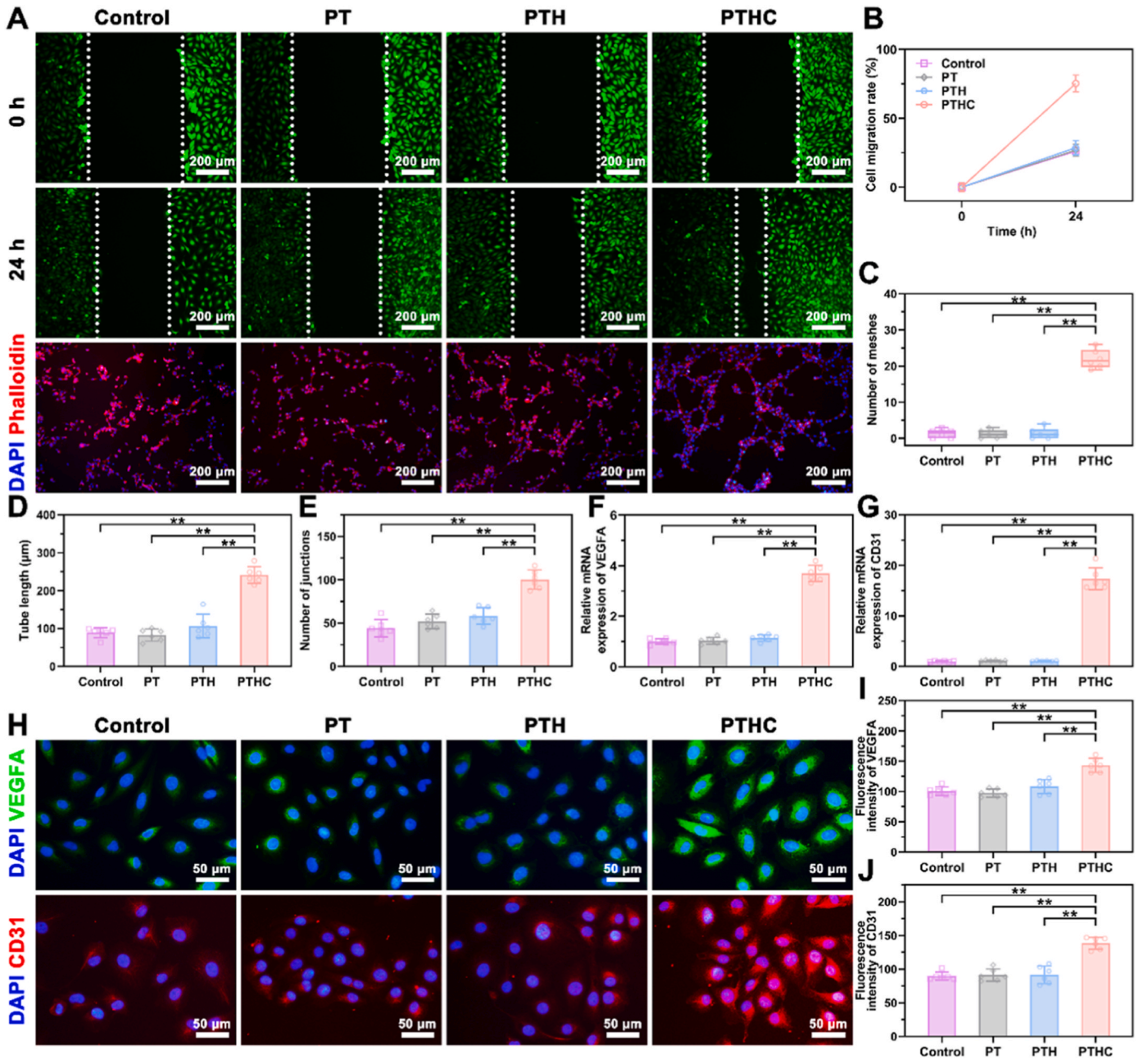

Fig. 3. Effect of hydrogels on angiogenesis *in vitro*. (A) Fluorescent images of HUVECs migration and tube formation treated with PT-based hydrogels. (B) Quantitative analysis of scratch healing assay. (C–E) Quantitative analysis of tube formation assay including the tube length, the number of meshes and junctions. (F, G) Expression of angiogenesis-related genes VEGFA and CD31. (H) IF staining images of angiogenic markers VEGFA (green) and CD31 (red) expression in HUVECs. (I, J) Quantitative analysis of VEGFA and CD31 fluorescence intensity. Data were represented as mean ± SD ($n = 6$); $^{*}p < 0.05$, $^{**}p < 0.01$ compared to each group.

were significantly increased, and PTHC hydrogels showed higher osteogenic activity (Fig. 4D–G). According to IF staining in Fig. 4H–J, it was observed that the expression of BMP2 and OCN in PTH and PTHC groups was increased, exhibiting a similar trend with qRT-PCR results. Meanwhile, compared with PTH hydrogel treatment, the PTHC hydrogel significantly promoted the BMP2 and OCN expression in BMSCs. These findings not only indicated that PTH and PTHC possessed superior osteogenic activity *in vitro*, but also confirmed CCG could synergistically improve osteogenic differentiation. As for osteogenic activity, both HA and CCG can promote osteogenic differentiation of BMSCs and accelerate bone regeneration [35–37]. In addition, CCG has been proven to upregulate VEGF and BMP2, inhibit osteoclasts, and regulate bone metabolism to improve osteoporosis [38–40].

Neural differentiation assay was conducted on NSCs to assess neurogenic activity *in vitro*. TUBB3 and MAP2 were known as the markers of early neurons and neuronal dendrites, which were used to label differentiated NSCs treated with hydrogels via IF staining in Fig. 5A. TUBB3 and MAP2 positive NSCs in the PTH and PTHC groups exhibited dendrite extension, especially the NSCs in the PTHC group were interconnected to form neural networks. Sholl analysis indicated that NSCs in the PTHC group had the highest degree of differentiation, and the dendritic length and neurite number of NSCs treated with PTH and PTHC hydrogels were significantly increased compared to the other groups (Fig. 5B–D). Also, as shown in Fig. 5E and F, the expression of TUBB3 and MAP2 on NSCs treated with PTH and PTHC hydrogels was significantly higher than that of the control and PT groups, suggesting that the PTH and PTHC hydrogels with neurogenic activity could improve the NSCs differentiation. In the neurogenic aspect, HA

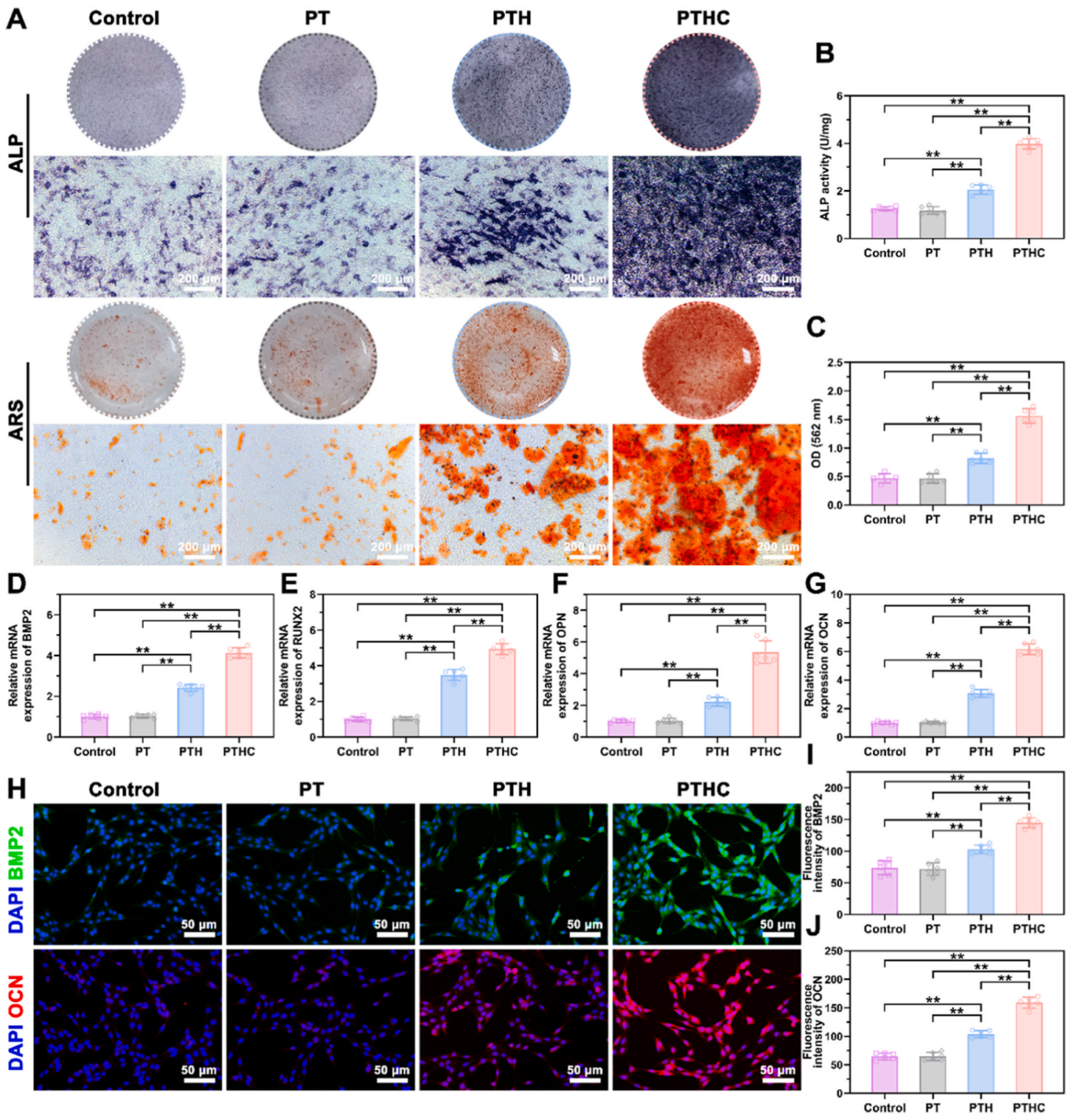

Fig. 4. Effect of hydrogels on osteogenic differentiation *in vitro*. (A) ALP and ARS staining of BMSCs treated with PT-based hydrogels for 7 and 14 days, respectively. (B, C) Quantitative analysis of ALP activity and ARS staining. (D–G) Osteogenesis-related genes BMP2, RUNX2, OPN, and OCN expression. (H) IF staining images of osteogenic markers BMP2 (green) and OCN (red) expression in BMSCs. (I, J) Quantitative analysis of BMP2 and OCN fluorescence intensity. Data were represented as mean ± SD ($n = 6$); $^{*}p < 0.05$, $^{**}p < 0.01$ compared to each group.

promoted neural differentiation and maturation of NSCs attributed to endocytosis and adhesion to cell membranes [15], while CCG with neuroprotection reduced the oxidative stress level after central nervous system injury [18,41]. Furthermore, ROS levels on the H_2O_2-induced HUVECs, BMSCs, and NSCs were determined by DCFH staining in Fig. 5G and H, the results manifested that PT-based hydrogels significantly inhibited H_2O_2-stimulated oxidative stress levels on the various cells. Particularly, the addition of CCG synergistically enhanced the antioxidant property of PTH hydrogel, demonstrating that the PTHC hydrogel could protect cells against oxidative stress.

3.3. Neuro-vascularized bone regeneration of PTHC hydrogel in vivo

After the establishment of the SD rat calvarial defect model, PT-based hydrogels were injected into the defect site *in situ* (Fig. 6A and S8). According to 3D reconstructed bone and blood vessels from the micro-

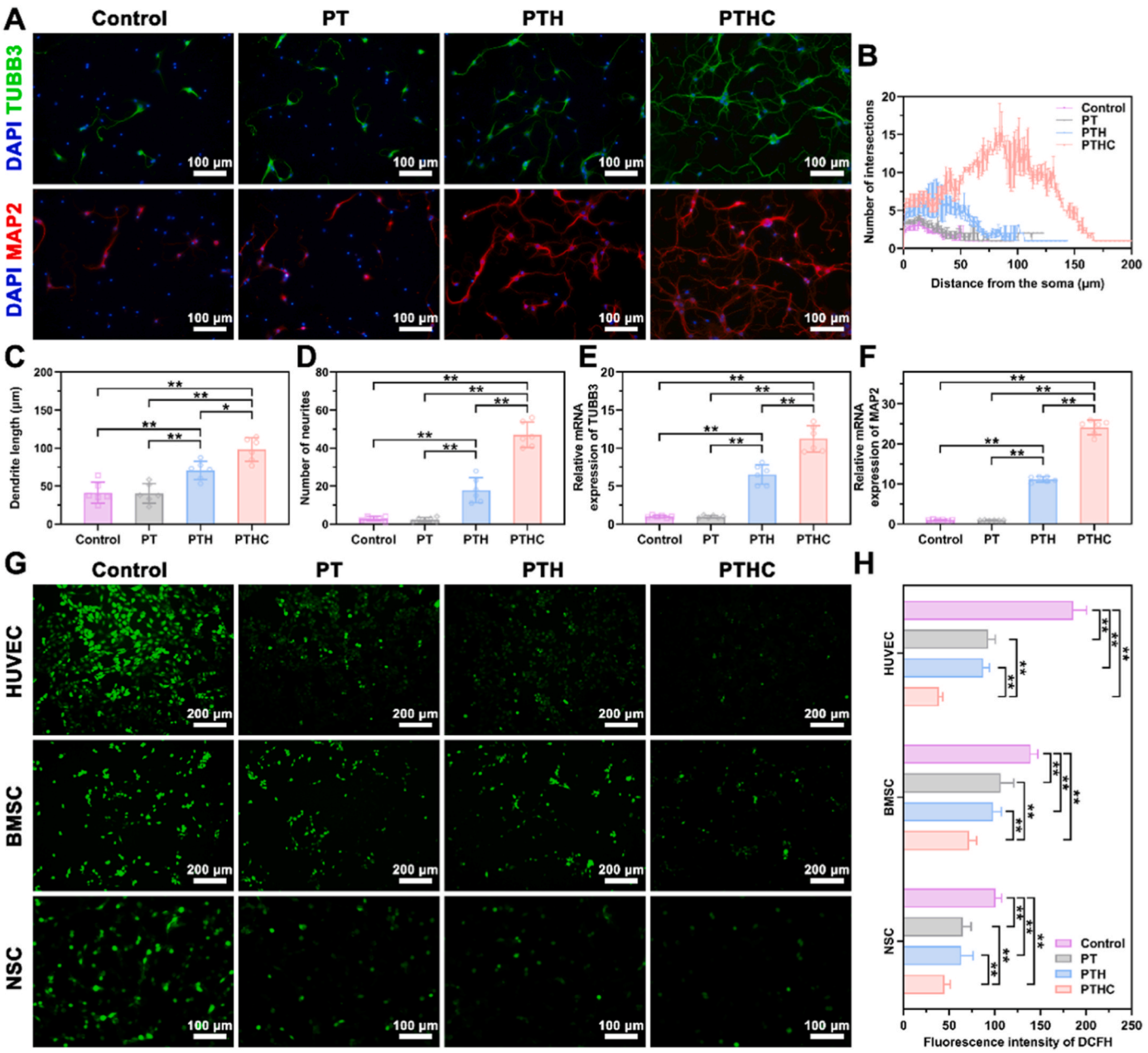

Fig. 5. Effect of hydrogels on neural differentiation and oxidative stress *in vitro*. (A) IF staining images of neurogenic markers TUBB3 (green) and MAP2 (red) expression in NSCs. (B–D) Quantitative analysis of neural differentiation assay including the Sholl analysis, dendrite length, and number of neurites. (E, F) Expression of neurogenesis-related genes TUBB3 and MAP2. (G) ROS levels (green) of H_2O_2-induced HUVECs, BMSCs, and NSCs treated with PT-based hydrogels. (H) Quantitative analysis of DCFH fluorescence intensity. Data were represented as mean ± SD ($n = 6$); $^*p < 0.05$, $^{**}p < 0.01$ compared to each group.

CT in Fig. 6B, the critical-sized defect in the control and PT groups still remained unhealed defect within 8 weeks, whereas bone regeneration occurred at the defect site in the PTHC group. Meanwhile, only a few blood vessels were observed at the defect site in the control, PT, and PTH groups. However, the PTHC hydrogel exhibited abundant angiogenesis *in vivo*. More importantly, these new blood vessels with a unique columnar structure were arranged in a linear shape and connected to each other by vascular arches, which were identified as type H blood vessels, a specific blood vessel subtype associated with the coupling of angiogenesis and osteogenesis [42,43]. As shown in Fig. 6C and D, compared with the control and PT groups, the percentage of bone/tissue volume (BV/TV) and bone mineral density (BMD) in the PTH and PTHC groups were significantly improved, and the highest BV/TV (33.46 ± 6.81 %) and BMD (0.30 ± 0.03 g/cm^3) were obtained in the PTHC hydrogel treatment. Meanwhile, bone trabecular parameters in Fig. S9 showed that the trabecular number (Tb. N) and trabecular thickness (Tb. Th) of the PTHC group was significantly enhanced, whereas the trabecular separation (Tb. Sp) of that was reduced, verifying the synergistic osteogenic effect of HA combined with CCG. Especially, the vascular volume at the defect site in the PTHC group increased to 7.82 ± 1.16 mm^3, which was notably larger than that in the control (2.15 ± 0.87 mm^3), PT (2.25 ± 0.94 mm^3), and PTH (2.73 ± 1.03 mm^3) groups (Fig. 6E). The above micro-CT analysis revealed that PTHC hydrogel could promote vascularized bone regeneration.

Histologically, biocompatibility was evaluated through histological analysis of vital organs *in vivo*. The H&E staining analysis in Figs. S10–14 showed that all the tissues including the liver, heart, spleen, lung, and kidney in each group kept normal morphology, indicating that PT-based hydrogels possessed good biocompatibility. Furthermore, as shown in Figs. S15A and B, the PT-based hydrogels degraded within 6 weeks of

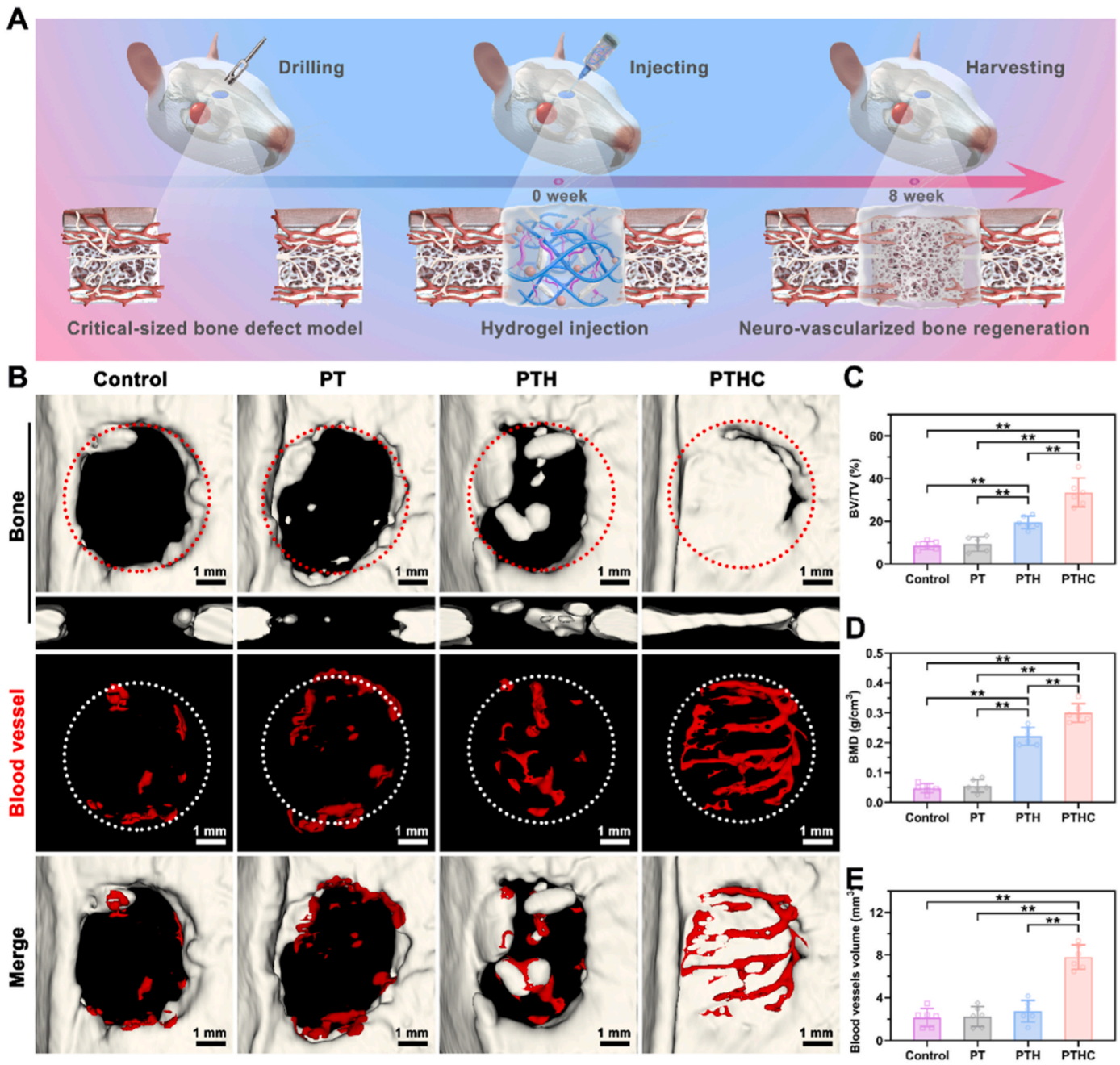

Fig. 6. Micro-CT analysis of bone regeneration *in vivo*. (A) Schematic diagram of critical-sized calvarial defect rat model and hydrogel injection. (B) Representative 3D reconstructed images of bone (transverse and coronal sections) and blood vessels in the defect sites. (C–E) Micro-CT quantification of BV/TV, BMD, and blood vessel volume after 8 weeks of hydrogel injection. Data were represented as mean ± SD ($n = 6$); $^{*}p < 0.05$, $^{**}p < 0.01$ compared to each group.

hydrogel injection *in vivo*, and this proper biodegradability did not cause foreign body occupying to hinder tissue regeneration. Also, H&E staining in Fig. S15C after 1 week of hydrogel injection showed that the PT-based hydrogels did not cause inflammation. Based on the H&E, Masson, and Goldner staining in Fig. 7A, A large amount of loose connective tissue was formed at the bone defect central site in the control and PT groups, including bundle collagen fibers and reticular elastic fibers. However, newly formed bone tissue was observed at the center of the defect in the PTH and PTHC groups. In particular, a large area of bone tissue and the collagen content (Fig. S16) were regenerated in the PTHC group, and dense collagen fibers were formed to connect the original and new bone tissue at the bone defect edge site. Meanwhile, as illustrated in Fig. 7B–D, the number of blood vessels, new bone area, and immature and mature bone in the PTHC group were significantly more than that of other groups. Additionally, the content of secretion including BMP2, OCN, VEGFA, PDGFB, BDNF, and CGRP in serum was detected in Fig. 7E–G. The results indicated that PTHC hydrogel significantly boosted the secretion level of BMP2, OCN, VEGFA, PDGFB, BDNF, and CGRP by 2.83, 1.66, 1.48, 2.42, 1.55, and 2.89 folds compared with the control group, respectively. CGRP is known as a neurotransmitter rich in the periosteal sensory nerve [44], which positively regulates vascular network reconstruction and bone regeneration [45–47].

Furthermore, IHC staining was conducted to evaluate the expression levels of BMP2 and OCN in Fig. 8A–C. The results indicated that BMP2 and OCN expressions in the PTH and PTHC groups were significantly higher than those in the control and PT groups, and the positive area ratios of BMP2 and OCN in the PTHC group were the highest in all

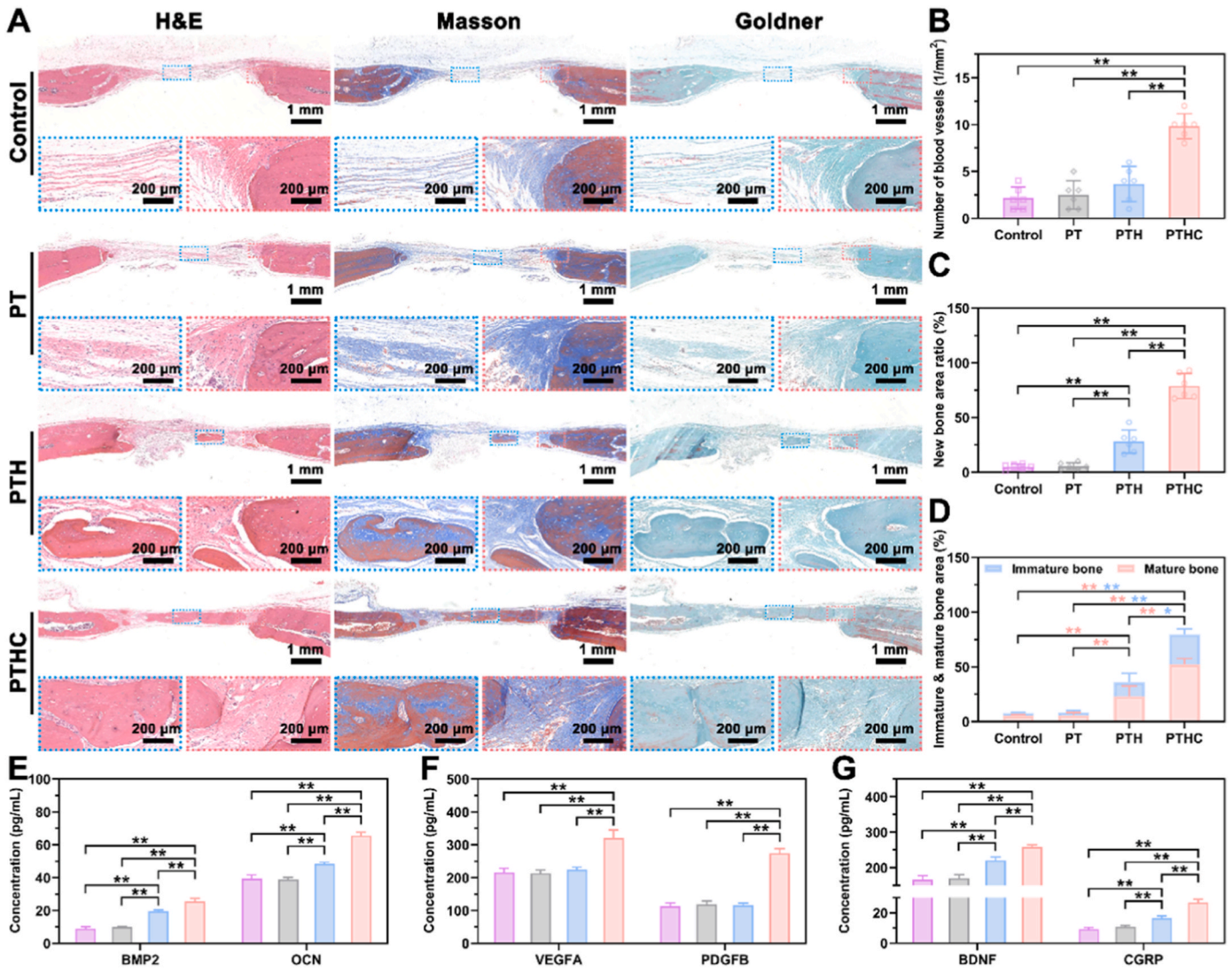

Fig. 7. Histological analysis of new bone formation *in vivo*. (A) Representative H&E, Masson, and Goldner staining (Blue dotted box: defect central site. Red dotted box: defect edge site). (B–D) Histological quantification of the number of blood vessels, the ratio of new bone area, and the proportion between immature and mature bone area. (E–G) The level of osteogenic, angiogenic, and neurogenic related indicators including BMP2, OCN, VEGFA, PDGFB, BDNF, and CGRP. Data were represented as mean ± SD ($n = 6$); *$p < 0.05$, **$p < 0.01$ compared to each group.

groups, reaching 76.97 ± 9.63 % and 82.71 ± 9.45 %, respectively. It was demonstrated that the PTHC hydrogel exhibited excellent osteogenesis *in vivo*, which was in accord with Masson and Goldner staining and ELISA detection. Simultaneously, IF co-staining was performed to investigate angiogenesis and neurogenesis *in vivo* (Fig. 8D–F). The results showed that the angiogenic-related CD31 and VEGFA positive area ratios in the PTHC group were 12.66 ± 3.25 % and 9.02 ± 2.81 %, which were significantly higher than those of the control, PT, and PTH groups. The VEGFA secretion and upregulated CD31 in the H-type vessels play an important role in the angiogenic and osteogenic coupling [48–50]. Obviously, it was confirmed that the PTH and PTHC hydrogels upregulated the expression of TUBB3 and MAP2, while CCG further enhanced neurogenesis *in vivo*, elucidating the secretion of CGRP was derived from TUBB3 and MAP2 marked sensory neurons. These abovementioned results demonstrated that PTHC hydrogel successfully reconstructed the microvascular network and enhanced vascular perfusion, accelerated sensory nerve repair and secreted neurotransmitters, improved bone injury microenvironment and achieved bone regeneration.

Transcriptome sequencing was further performed on bone tissues to explore the underlying mechanism of PTHC hydrogel for neurovascularized bone regeneration. According to the Pearson correlation heatmap in Fig. 9A, repetition per group exhibited high consistency ($0.990 < R^2 < 1$ for the control group, and $0.998 < R^2 < 1$ for the PTHC group). Principal component analysis revealed distinct transcriptomic profiles between control and PTHC groups (Fig. 9B). Volcano plot showed that there were 122 upregulated and 245 downregulated DEGs in the comparison between the control and PTHC groups (Fig. 9C). After cluster analysis, the heatmap displayed the expression levels of all DEGs (Fig. 9D). In particular, heatmaps and PPI networks of osteogenesis, angiogenesis, and neurogenesis related DEGs and proteins were exhibited in Fig. 9E–F. The results indicated that the treatment of PTHC hydrogel could upregulate the expression of osteogenic related genes including RUNX2, BMP2, and bone gamma-carboxyglutamate protein (BGLAP, also called OCN). Also, PTHC hydrogel increased the expression of angiogenic related genes such as VEGFA, PDGFA, and PDGFB, which were involved in coupling angiogenesis and osteogenesis [48,51]. Moreover, the PTHC hydrogel upregulated the expression of TUBB3, MAP2, BDNF, and calcitonin-related polypeptide alpha (CALCA, also known as CGRP). There was evidence that sensory nerves and neuropeptide CGRP contributed to bone healing [52,53]. PPI networks illuminated that the key proteins such as RUNX2, BMP2, and collagen type I

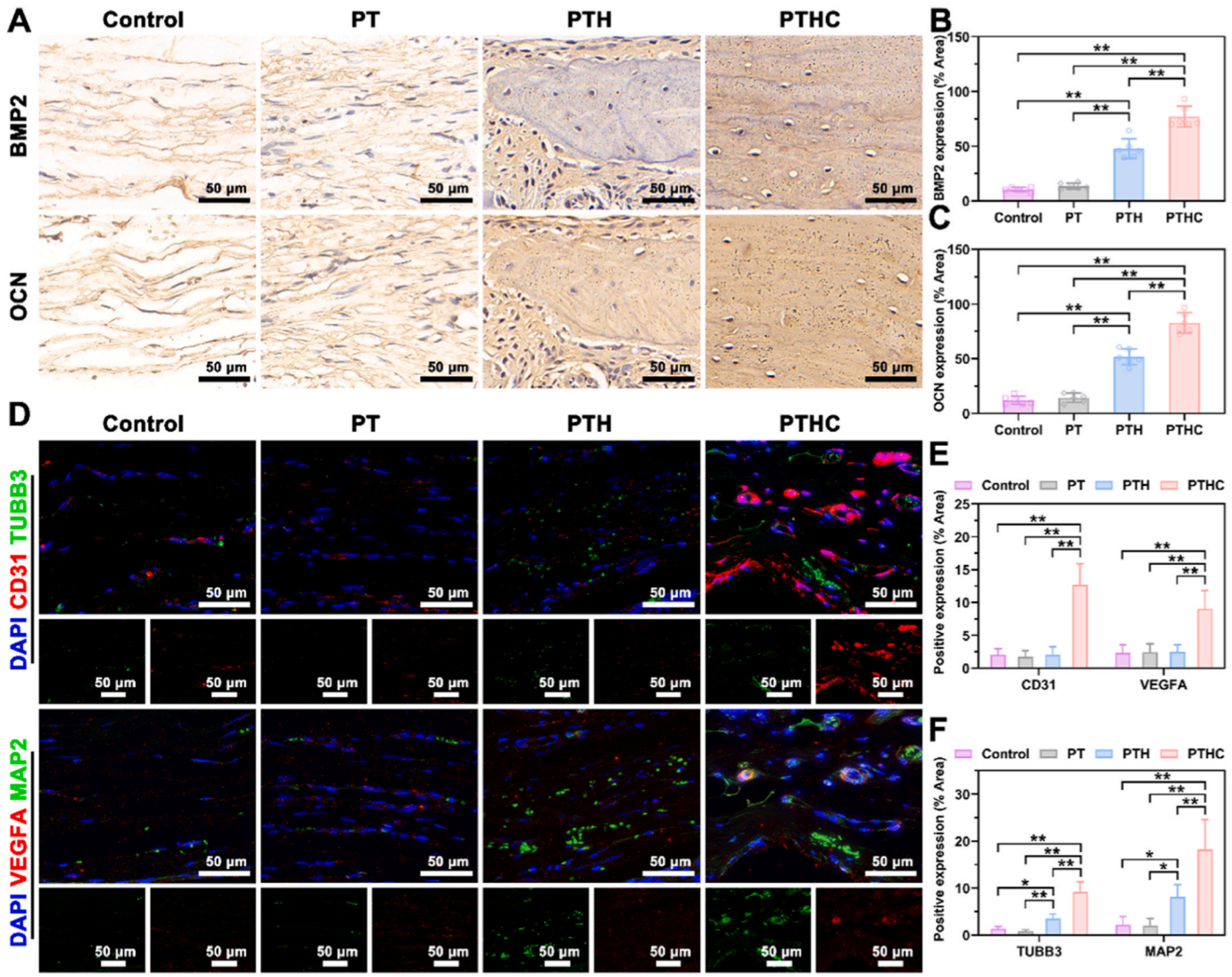

Fig. 8. Immunostaining analysis of neuro-vascularized bone regeneration *in vivo*. (A) IHC staining of BMP2 and OCN expression after hydrogel injection in calvarial defect sites. (B, C) Quantitative analysis of BMP2 and OCN positive area. (D) IF co-staining of blood vessels (CD31 and VEGFA, red) and nerves (TUBB3 and MAP2, green). (E, F) Quantitative analysis of CD31, VEGFA, TUBB3, and MAP2 positive area. Data were represented as mean ± SD ($n = 6$); $^{*}p < 0.05$, $^{**}p < 0.01$ compared to each group.

alpha 1 (COL1A1) mainly participate in molecular interactions during osteogenesis. Additionally, interactive webs involved angiogenesis-related proteins like VEGFA, PDGFB, and fibroblast growth factor 21 (FGF21), as well as neurogenesis-related proteins including TUBB3, MAP2, and BDNF, which was essential for the coordinated process of neuro-vascularized bone repair. The dynamic interplay among these proteins emphasized intricate cell communication and complex bone regeneration [54]. As shown in Fig. 9G, the key GO terms associated with osteogenesis, angiogenesis, and neurogenesis were enriched, involving positive regulation of bone resorption, osteoblast differentiation, positive regulation of cell migration, angiogenesis, neuron projection, and neuronal cell body. Meanwhile, KEGG pathway enrichment analysis showed that the PI3K/Akt pathway is the most significantly enriched signaling pathway (Fig. 9H). Furthermore, the expression levels of the PI3K/Akt pathway were detected using WB assay to verify the mechanism of PTHC hydrogel. As shown in Fig. S17, the expression of p-PI3K and p-Akt in the bone tissues of the PTHC group was significantly upregulated, indicating the activation of the PI3K/Akt pathway. The PI3K/Akt signaling pathway plays a crucial role in regulating cell proliferation, differentiation, migration, and various other cellular biological processes [55,56]. Moreover, the activation of the PI3K/Akt pathway is involved in the occurrence and progression of bone regeneration and BMSCs-mediated angiogenesis [57–59]. Notably, PTHC hydrogel could activate the PI3K/Akt signaling pathway and facilitate the bone microenvironment, thereby promoting neuro-vascularized bone regeneration.

4. Conclusion

Collectively, this study provides a controllable drug release strategy using a pH and ROS dual-responsive hydrogel for neuro-vascularized bone regeneration. Injectable PT-based hydrogel scavenges ROS, and the on-demand release of HA and CCG promotes NSC differentiation and coupling of angiogenesis and osteogenesis, thereby reconstructing the microvascular network, accelerating sensory nerve repair, improving injury microenvironment for bone regeneration. Overall, our study demonstrated the therapeutic effect of multi-bioactive PTHC hydrogel on critical-sized bone defects and developed a responsive bioactive delivery platform with promising prospects for clinical application that could adapt the loaded substance and responsivity to demand.

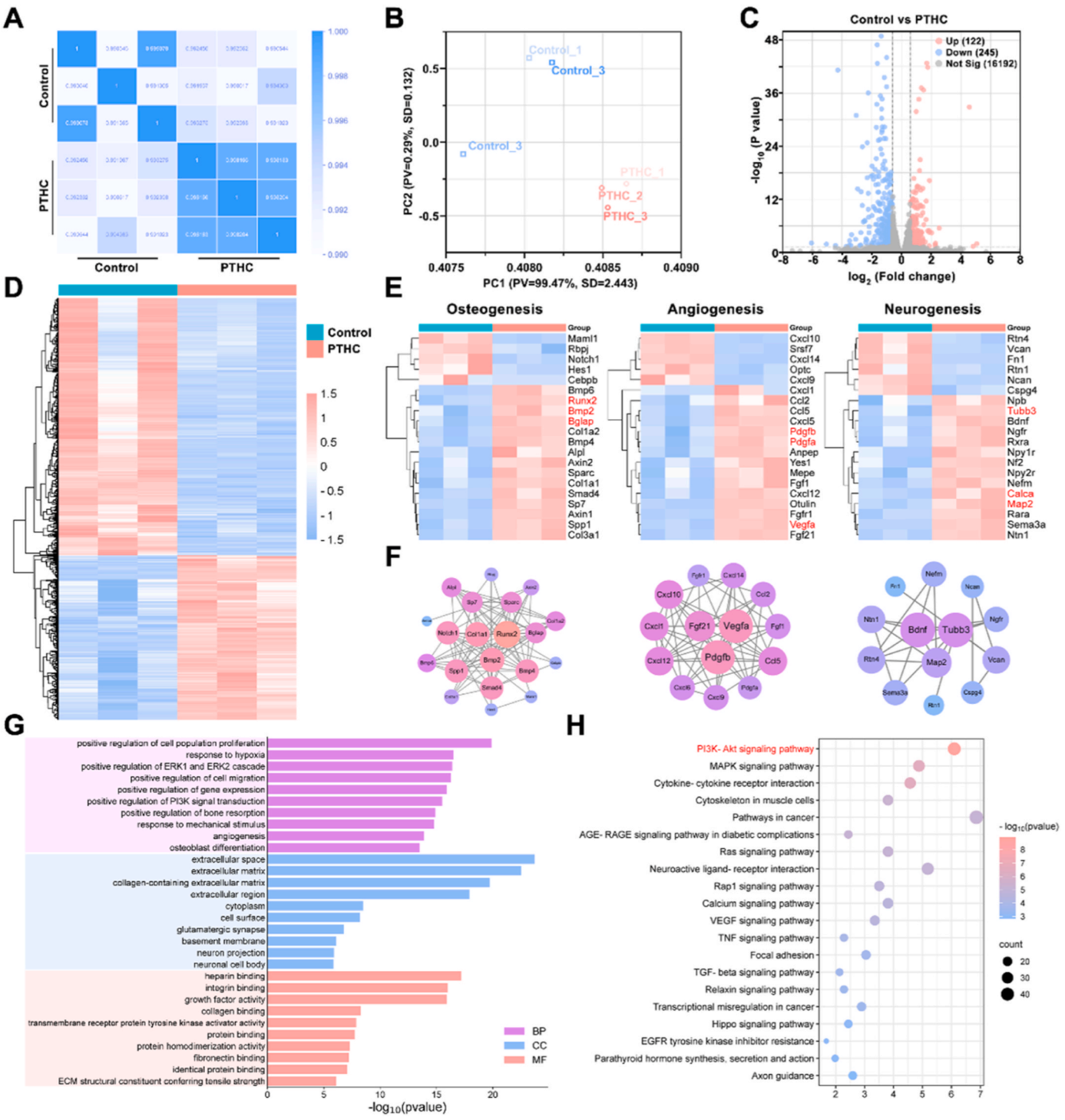

Fig. 9. Mechanism of PTHC hydrogel on neuro-vascularized bone regeneration *in vivo*. (A) Pearson correlation heatmap of control and PTHC groups. (B) Principal component analysis between control and PTHC groups. (C) Venn plot of DEGs. (D–F) Heatmap based on all DEGs from control and PTHC groups. Heatmap and PPI networks of key DEGs associated with the osteogenesis, angiogenesis, and neurogenesis. (G) GO analysis enriched terms in biological process (BP), cellular component (CC), and molecular function (MF) categories. (H) KEGG pathway enrichment analysis.

CRediT authorship contribution statement

Wanshun Wang: Writing – original draft, Visualization, Methodology, Investigation, Formal analysis, Data curation, Conceptualization. **Hu Chen:** Methodology, Investigation, Formal analysis, Data curation. **Jiacong Xiao:** Software, Resources, Formal analysis, Data curation. **Dan Luo:** Resources, Methodology, Investigation, Formal analysis. **Yonghui Hou:** Supervision, Software, Resources. **Jiheng Zhan:** Validation, Supervision, Funding acquisition. **Yu Hou:** Supervision. **Xing Li:** Supervision. **Huili Yang:** Investigation, Formal analysis, Data curation. **Shudong Chen:** Supervision, Funding acquisition. **Dingkun Lin:** Resources, Project administration, Funding acquisition.

Declaration of competing interest

The authors declare that they have no known competing financial

interests or personal relationships that could have appeared to influence the work reported in this paper.

Acknowledgments

Wanshan Wang, Hu Chen, and Jiacong Xiao contributed equally to this work. This research was financially supported by the National Natural Science Foundation of China (82074451; 81704095; 82104895), the Guangzhou Science and Technology Planning Project (202102020542), the China Postdoctoral Science Foundation (2021M700905), and the Science and Technology Program of Guangzhou (202201010974). The authors would like to thank Shiyanjia Lab (www.shiyanjia.com) for the SEM and FTIR analysis.

Appendix A. Supplementary data

Supplementary data to this article can be found online at https://doi.org/10.1016/j.mtbio.2024.101369.

Data availability

Data will be made available on request.

References

[1] S. Ankit, S. Harsh N, L. Benjamin, L. Michael T, Mechanisms of bone development and repair, Nat. Rev. Mol. Cell. Bio. 21 (11) (2020), https://doi.org/10.1038/s41580-020-00279-w.
[2] C. V, M. G, P. E, B. M, C. C, S. G, L. W, L. G, Bone substitutes in orthopaedic surgery: from basic science to clinical practice, J. Mater. Sci-Mater. M. 25 (10) (2014), https://doi.org/10.1007/s10856-014-5240-2.
[3] F. Michael A, S. Wade R, M. Cyril, I. Kaan, W. Allison E, R. Erin, P. Gabrielle, H. David J, S. Philip F, Outcomes and complication rates of different bone grafting modalities in long bone fracture nonunions: a retrospective cohort study in 182 patients, J. Orthop. Surg. Res. 8 (0) (2013), https://doi.org/10.1186/1749-799x-8-33.
[4] N.G. Schwartz, A.C. Hernandez-Romieu, P. Annambhotla, T.D. Filardo, S. P. Althomsons, R.J. Free, R. Li, W.W. Wilson, M. Deutsch-Feldman, M. Drees, Nationwide tuberculosis outbreak in the USA linked to a bone graft product: an outbreak report, Lancet Infect. Dis. 22 (11) (2022) 1617–1625, https://doi.org/10.1016/S1473-3099(22)00425-X.
[5] G. Walters, I. Pountos, P.V. Giannoudis, The cytokines and micro-environment of fracture haematoma: current evidence, J. Tissue. Eng. Regen. M. 12 (3) (2018) e1662–e1677, https://doi.org/10.1002/term.2593.
[6] J. Li, F. Han, J. Ma, H. Wang, J. Pan, G. Yang, H. Zhao, J. Zhao, J. Liu, Z. Liu, B. Li, Targeting endogenous hydrogen peroxide at bone defects promotes bone repair, Adv. Funct. Mater. 32 (10) (2022) 2111208, https://doi.org/10.1002/adfm.202111208.
[7] H. Sun, J. Xu, Y. Wang, S. Shen, X. Xu, L. Zhang, Q. Jiang, Bone microenvironment regulative hydrogels with ROS scavenging and prolonged oxygen-generating for enhancing bone repair, Bioact. Mater. 24 (2023) 477–496, https://doi.org/10.1016/j.bioactmat.2022.12.021.
[8] W. Wang, K.W.K. Yeung, Bone grafts and biomaterials substitutes for bone defect repair: a review, Bioact. Mater. 2 (4) (2018), https://doi.org/10.1016/j.bioactmat.2017.05.007.
[9] L. Diana, M.-C. Cláudia, O. Mariana B, M. João F, Bone physiology as inspiration for tissue regenerative therapies, Biomaterials 185 (0) (2018), https://doi.org/10.1016/j.biomaterials.2018.09.028.
[10] P.I. Mapp, D.A. Walsh, Mechanisms and targets of angiogenesis and nerve growth in osteoarthritis, Nat. Rev. Rheumatol. 8 (7) (2012) 390–398, https://doi.org/10.1038/nrrheum.2012.80.
[11] Q. Qin, S. Lee, N. Patel, K. Walden, M. Gomez-Salazar, B. Levi, A.W. James, Neurovascular coupling in bone regeneration, Exp. Mol. Med. 54 (11) (2022) 1844–1849, https://doi.org/10.1038/s12276-022-00899-6.
[12] S. Mary H, W. Jennifer L, H. John R, T. Jan K, Soft-tissue vessels and cellular preservation in Tyrannosaurus rex, Science 307 (5717) (2005), https://doi.org/10.1126/science.1108397.
[13] J. Li, Z. Zhang, J. Tang, Z. Hou, L. Li, B. Li, Emerging roles of nerve-bone axis in modulating skeletal system, Med. Res. Rev. 44 (4) (2024) 1867–1903, https://doi.org/10.1002/med.22031.
[14] J. He, M. Hao, J. Duan, H. Xia, W. Li, H. Xue, S. Wang, W. Liu, D. Li, Y. Sang, Synergistic effect of endocellular calcium ion release and nanotopograpy of one-dimensional hydroxyapatite nanomaterials for accelerating neural stem cell differentiation, Compos. Part B-Eng. 219 (2021) 108944, https://doi.org/10.1016/j.compositesb.2021.108944.
[15] M. Hao, Z. Zhang, C. Liu, Y. Tian, J. Duan, J. He, Z. Sun, H. Xia, S. Zhang, S. Wang, Y. Sang, G. Xing, H. Liu, Hydroxyapatite nanorods function as safe and effective growth factors regulating neural differentiation and neuron development, Adv. Mater. 33 (33) (2021) e2100895, https://doi.org/10.1002/adma.202100895.
[16] I.I. Hejazi, R. Khanam, S.H. Mehdi, A.R. Bhat, M.M.A. Rizvi, S.C. Thakur, F. Athar, Antioxidative and anti-proliferative potential of Curculigo orchioides Gaertn in oxidative stress induced cytotoxicity: in vitro, ex vivo and in silico studies, Food Chem. Toxicol. 115 (2018) 244–259, https://doi.org/10.1016/j.fct.2018.03.013.
[17] L. Wang, Y.J. He, T. Han, L. Zhao, L. Lv, Y.Q. He, Q.Y. Zhang, H.L. Xin, Metabolites of curculigoside in rats and their antiosteoporotic activities in osteoblastic MC3T3-E1 cells, Fitoterapia 117 (2017) 109–117, https://doi.org/10.1016/j.fitote.2017.01.009.
[18] Z. Tian, W. Yu, H.B. Liu, N. Zhang, X.B. Li, M.G. Zhao, S.B. Liu, Neuroprotective effects of curculigoside against NMDA-induced neuronal excitoxicity in vitro, Food Chem. Toxicol. 50 (11) (2012) 4010–4015, https://doi.org/10.1016/j.fct.2012.08.006.
[19] T. Chen, Q. Tu, L. Cheng, Z. Li, D. Lin, Effects of curculigoside A on random skin flap survival in rats, Eur. J. Pharmacol. 834 (2018) 281–287, https://doi.org/10.1016/j.ejphar.2018.07.030.
[20] B. Zhang, W. Wang, P. Gao, X. Li, L. Chen, Z. Lin, H. Chen, W. Liang, Z. Kong, D. Lin, X. Wu, T. Zhang, Injectable, electroconductive, free radical scavenging silk fibroin/black phosphorus/glycyrrhizic acid nanocomposite hydrogel for enhancing spinal cord repair, Adv. Healthc. Mater. 13 (18) (2024) e2304300, https://doi.org/10.1002/adhm.202304300.
[21] H. Yang, W. Wang, J. Xiao, R. Yang, L. Feng, H. Xu, L. Xu, Y. Xing, ROS-responsive injectable hydrogels loaded with exosomes carrying miR-4500 reverse liver fibrosis, Biomaterials 314 (2024) 122887, https://doi.org/10.1016/j.biomaterials.2024.122887.
[22] W. Wang, X. Cheng, J. Liao, Z. Lin, L. Chen, D. Liu, T. Zhang, L. Li, Y. Lu, H. Xia, Synergistic photothermal and photodynamic therapy for effective implant-related bacterial infection elimination and biofilm disruption using Cu(9)S(8) nanoparticles, ACS Biomater. Sci. Eng. 5 (11) (2019) 6243–6253, https://doi.org/10.1021/acsbiomaterials.9b01280.
[23] W. Wang, B. Li, H. Yang, Z.F. Lin, L. Chen, Z. Li, J. Ge, T. Zhang, H. Xia, L. Li, Y. Lu, Efficient elimination of multidrug-resistant bacteria using copper sulfide nanozymes anchored to graphene oxide nanosheets, Nano Res. 13 (8) (2020) 2156–2164, https://doi.org/10.1007/s12274-020-2824-7.
[24] J. Zhang, X. Ye, W. Li, Z. Lin, W. Wang, L. Chen, Q. Li, X. Xie, X. Xu, Y. Lu, Copper-containing chitosan-based hydrogels enabled 3D-printed scaffolds to accelerate bone repair and eliminate MRSA-related infection, Int. J. Biol. Macromol. 240 (2023) 124463, https://doi.org/10.1016/j.ijbiomac.2023.124463.
[25] T. Wu, B. Li, W. Wang, L. Chen, Z. Li, M. Wang, Z. Zha, Z. Lin, H. Xia, T. Zhang, Strontium-substituted hydroxyapatite grown on graphene oxide nanosheet-reinforced chitosan scaffold to promote bone regeneration, Biomater. Sci. 8 (16) (2020) 4603–4615, https://doi.org/10.1039/d0bm00523a.
[26] Z. He, C. Sun, Y. Ma, X. Chen, Y. Wang, K. Chen, F. Xie, Y. Zhang, Y. Yuan, C. Liu, Rejuvenating aged bone repair through multihierarchy reactive oxygen species-regulated hydrogel, Adv. Mater. 36 (9) (2024) e2306552, https://doi.org/10.1002/adma.202306552.
[27] L. Zhou, D. Chen, R. Wu, L. Li, T. Shi, Z. Shangguang, H. Lin, G. Chen, Z. Wang, W. Liu, An injectable and photocurable methacrylate-silk fibroin/nano-hydroxyapatite hydrogel for bone regeneration through osteoimmunomodulation, Int. J. Biol. Macromol. 263 (Pt 1) (2024) 129925, https://doi.org/10.1016/j.ijbiomac.2024.129925.
[28] H. Yook, J. Hwang, W. Yeo, J. Bang, J. Kim, T.Y. Kim, J.S. Choi, J.W. Han, Design strategies for hydroxyapatite-based materials to enhance their catalytic performance and applicability, Adv. Mater. 35 (43) (2023) e2204938, https://doi.org/10.1002/adma.202204938.
[29] Y. Zhao, Z. Cui, B. Liu, J. Xiang, D. Qiu, Y. Tian, X. Qu, Z. Yang, An injectable strong hydrogel for bone reconstruction, Adv. Healthc. Mater. 8 (17) (2019) e1900709, https://doi.org/10.1002/adhm.201900709.
[30] J. Fang, P. Li, X. Lu, L. Fang, X. Lü, F. Ren, A strong, tough, and osteoconductive hydroxyapatite mineralized polyacrylamide/dextran hydrogel for bone tissue regeneration, Acta Biomater. 88 (2019) 503–513, https://doi.org/10.1016/j.actbio.2019.02.019.
[31] Z.C. Hu, J.Q. Lu, T.W. Zhang, H.F. Liang, H. Yuan, D.H. Su, W. Ding, R.X. Lian, Y. X. Ge, B. Liang, J. Dong, X.G. Zhou, L.B. Jiang, Piezoresistive MXene/silk fibroin nanocomposite hydrogel for accelerating bone regeneration by re-establishing electrical microenvironment, Bioact. Mater. 22 (2023) 1–17, https://doi.org/10.1016/j.bioactmat.2022.08.025.
[32] Z. Mao, X. Bi, C. Yu, L. Chen, J. Shen, Y. Huang, Z. Wu, H. Qi, J. Guan, X. Shu, B. Yu, Y. Zheng, Mechanically robust and personalized silk fibroin-magnesium composite scaffolds with water-responsive shape-memory for irregular bone regeneration, Nature Commun 15 (1) (2024) 4160, https://doi.org/10.1038/s41467-024-48417-8.
[33] M. Wu, H. Liu, D. Li, Y. Zhu, P. Wu, Z. Chen, F. Chen, Y. Chen, Z. Deng, L. Cai, Smart-responsive multifunctional therapeutic system for improved regenerative microenvironment and accelerated bone regeneration via mild photothermal therapy, Adv. Sci. 11 (2) (2024) e2304641, https://doi.org/10.1002/advs.202304641.
[34] X. Li, K. Xu, Y. He, B. Tao, K. Li, C. Lin, J. Hu, J. Wu, Y. Wu, S. Liu, P. Liu, H. Wang, K. Cai, ROS-responsive hydrogel coating modified titanium promotes vascularization and osteointegration of bone defects by orchestrating immunomodulation, Biomaterials 287 (2022) 121683, https://doi.org/10.1016/j.biomaterials.2022.121683.
[35] Q. Shen, D. Zeng, Y. Zhou, L. Xia, Y. Zhao, G. Qiao, L. Xu, Y. Liu, Z. Zhu, X. Jiang, Curculigoside promotes osteogenic differentiation of bone marrow stromal cells

from ovariectomized rats, J. Pharm. Pharmacol. 65 (7) (2013) 1005–1013, https://doi.org/10.1111/jphp.12054.
[36] R. Yang, B. Chen, X. Zhang, Z. Bao, Q. Yan, S. Luan, Degradable nanohydroxyapatite-reinforced superglue for rapid bone fixation and promoted osteogenesis, ACS Nano 18 (11) (2024) 8517–8530, https://doi.org/10.1021/acsnano.4c01214.
[37] L. Tong, X. Pu, Q. Liu, X. Li, M. Chen, P. Wang, Y. Zou, G. Lu, J. Liang, Y. Fan, X. Zhang, Y. Sun, Nanostructured 3D-printed hybrid scaffold accelerates bone regeneration by photointegrating nanohydroxyapatite, Adv. Sci. 10 (13) (2023) e2300038, https://doi.org/10.1002/advs.202300038.
[38] C. Ma, J. Zhang, J. Fu, L. Cheng, G. Zhao, Y. Gu, Up-regulation of VEGF by MC3T3-E1 cells treated with curculigoside, Phytother Res. 25 (6) (2011) 922–926, https://doi.org/10.1002/ptr.3449.
[39] M. Liu, S. Liu, Q. Zhang, Y. Fang, Y. Yu, L. Zhu, Y. Liu, W. Gong, L. Zhao, L. Qin, Q. Zhang, Curculigoside attenuates oxidative stress and osteoclastogenesis via modulating Nrf2/NF-κB signaling pathway in RAW264.7 cells, J. Ethnopharmacol. 275 (2021) 114129, https://doi.org/10.1016/j.jep.2021.114129.
[40] W.L. You, Z.L. Xu, Curculigoside promotes osteogenic differentiation of ADSCs to prevent ovariectomized-induced osteoporosis, J. Orthop. Surg. Res. 16 (1) (2021) 279, https://doi.org/10.1186/s13018-021-02389-3.
[41] Y. Xu, K. Wen, A. Liu, X. Wang, H. Xu, H. Wen, Efficacy of curculigoside in protecting against ischemic brain injury through regulation of oxidative stress and NF-κB and PI3K/Akt expression, J. Ethnopharmacol. 301 (2023) 115804, https://doi.org/10.1016/j.jep.2022.115804.
[42] A.P. Kusumbe, S.K. Ramasamy, R.H. Adams, Coupling of angiogenesis and osteogenesis by a specific vessel subtype in bone, Nature 507 (7492) (2014) 323–328, https://doi.org/10.1038/nature13145.
[43] T. Deng, W. Lu, X. Zhao, H. Wang, Y. Zheng, A. Zheng, Z. Shen, Chondroitin sulfate/silk fibroin hydrogel incorporating graphene oxide quantum dots with photothermal-effect promotes type H vessel-related wound healing, Carbohydr. Polym. 334 (2024) 121972, https://doi.org/10.1016/j.carbpol.2024.121972.
[44] X. Zhao, G. Wu, J. Zhang, Z. Yu, J. Wang, Activation of CGRP receptor-mediated signaling promotes tendon-bone healing, Sci. Adv. 10 (10) (2024) eadg7380, https://doi.org/10.1126/sciadv.adg7380.
[45] L. Ye, J. Xu, J. Mi, X. He, Q. Pan, L. Zheng, H. Zu, Z. Chen, B. Dai, X. Li, Q. Pang, L. Zou, L. Zhou, L. Huang, W. Tong, G. Li, L. Qin, Biodegradable magnesium combined with distraction osteogenesis synergistically stimulates bone tissue regeneration via CGRP-FAK-VEGF signaling axis, Biomaterials 275 (2021) 120984, https://doi.org/10.1016/j.biomaterials.2021.120984.
[46] J. Mi, J.K. Xu, Z. Yao, H. Yao, Y. Li, X. He, B.Y. Dai, L. Zou, W.X. Tong, X.T. Zhang, P.J. Hu, Y.C. Ruan, N. Tang, X. Guo, J. Zhao, J.F. He, L. Qin, Implantable electrical stimulation at dorsal root ganglions accelerates osteoporotic fracture healing via calcitonin gene-related peptide, Adv. Sci. 9 (1) (2022) e2103005, https://doi.org/10.1002/advs.202103005.
[47] Y. Zhang, J. Xu, Y.C. Ruan, M.K. Yu, M. O'Laughlin, H. Wise, D. Chen, L. Tian, D. Shi, J. Wang, S. Chen, J.Q. Feng, D.H. Chow, X. Xie, L. Zheng, L. Huang, S. Huang, K. Leung, N. Lu, L. Zhao, H. Li, D. Zhao, X. Guo, K. Chan, F. Witte, H. C. Chan, Y. Zheng, L. Qin, Implant-derived magnesium induces local neuronal production of CGRP to improve bone-fracture healing in rats, Nat. Med. 22 (10) (2016) 1160–1169, https://doi.org/10.1038/nm.4162.
[48] Y. Peng, S. Wu, Y. Li, J.L. Crane, Type H blood vessels in bone modeling and remodeling, Theranostics 10 (1) (2020) 426–436, https://doi.org/10.7150/thno.34126.
[49] Y. Han, X. You, W. Xing, Z. Zhang, W. Zou, Paracrine and endocrine actions of bone-the functions of secretory proteins from osteoblasts, osteocytes, and osteoclasts, Bone Res 6 (2018) 16, https://doi.org/10.1038/s41413-018-0019-6.
[50] H. Xie, Z. Cui, L. Wang, Z. Xia, Y. Hu, L. Xian, C. Li, L. Xie, J. Crane, M. Wan, G. Zhen, Q. Bian, B. Yu, W. Chang, T. Qiu, M. Pickarski, L.T. Duong, J.J. Windle, X. Luo, E. Liao, X. Cao, PDGF-BB secreted by preosteoclasts induces angiogenesis during coupling with osteogenesis, Nat. Med. 20 (11) (2014) 1270–1278, https://doi.org/10.1038/nm.3668.
[51] F. Tao, Y. Cheng, X. Shi, H. Zheng, Y. Du, W. Xiang, H. Deng, Applications of chitin and chitosan nanofibers in bone regenerative engineering, Carbohydr. Polym. 230 (2020) 115658, https://doi.org/10.1016/j.carbpol.2019.115658.
[52] Y. Xu, C. Xu, K. Yang, L. Ma, G. Li, Y. Shi, X. Feng, L. Tan, D. Duan, Z. Luo, C. Yang, Copper ion-modified germanium phosphorus nanosheets integrated with an electroactive and biodegradable hydrogel for neuro-vascularized bone regeneration, Adv. Healthc. Mater. 12 (27) (2023) e2301151, https://doi.org/10.1002/adhm.202301151.
[53] J. Appelt, A. Baranowsky, D. Jahn, T. Yorgan, P. Köhli, E. Otto, S.K. Farahani, F. Graef, M. Fuchs, A. Herrera, M. Amling, T. Schinke, K.H. Frosch, G.N. Duda, S. Tsitsilonis, J. Keller, The neuropeptide calcitonin gene-related peptide alpha is essential for bone healing, EBioMedicine 59 (2020) 102970, https://doi.org/10.1016/j.ebiom.2020.102970.
[54] J. Wang, Y. Wu, G. Li, F. Zhou, X. Wu, M. Wang, X. Liu, H. Tang, L. Bai, Z. Geng, P. Song, Z. Shi, X. Ren, J. Su, Engineering large-scale self-mineralizing bone organoids with bone matrix-inspired hydroxyapatite hybrid bioinks, Adv. Mater. 36 (30) (2024) e2309875, https://doi.org/10.1002/adma.202309875.
[55] S. Miao, J. Zhou, B. Liu, X. Lei, T. Wang, X. Hao, P. Cheng, H. Wu, Y. Song, G. Pei, L. Bi, A 3D bioprinted nano-laponite hydrogel construct promotes osteogenesis by activating PI3K/AKT signaling pathway, Mater. Today Bio 16 (2022) 100342, https://doi.org/10.1016/j.mtbio.2022.100342.
[56] J. Yang, L. Zhang, Y. Wang, N. Wang, H. Wei, S. Zhang, Q. Ding, S. Sun, C. Ding, W. Liu, Dihydromyricetin-loaded oxidized polysaccharide/L-arginine chitosan adhesive hydrogel promotes bone regeneration by regulating PI3K/AKT signaling pathway and MAPK signaling pathway, Carbohydr. Polym. 346 (2024) 122614, https://doi.org/10.1016/j.carbpol.2024.122614.
[57] S. Zhou, C. Xiao, L. Fan, J. Yang, R. Ge, M. Cai, K. Yuan, C. Li, R.W. Crawford, Y. Xiao, P. Yu, C. Deng, C. Ning, L. Zhou, Y. Wang, Injectable ultrasound-powered bone-adhesive nanocomposite hydrogel for electrically accelerated irregular bone defect healing, J. Nanobiotechnol. 22 (1) (2024) 54, https://doi.org/10.1186/s12951-024-02320-y.
[58] J. Long, Z. Yao, W. Zhang, B. Liu, K. Chen, L. Li, B. Teng, X.F. Du, C. Li, X.F. Yu, L. Qin, Y. Lai, Regulation of osteoimmune microenvironment and osteogenesis by 3D-printed PLAG/black phosphorus scaffolds for bone regeneration, Adv. Sci. 10 (28) (2023) e2302539, https://doi.org/10.1002/advs.202302539.
[59] L. Deng, M. Hou, N. Lv, Q. Zhou, X. Hua, X. Hu, X. Ge, X. Zhu, Y. Xu, H. Yang, X. Chen, H. Liu, F. He, Melatonin-encapsuled silk fibroin electrospun nanofibers promote vascularized bone regeneration through regulation of osteogenesis-angiogenesis coupling, Mater. Today Bio 25 (2024) 100985, https://doi.org/10.1016/j.mtbio.2024.100985.